

# On the Ability of Deep Networks to Learn Symmetries from Data: A Neural Kernel Theory

Andrea Perin<sup>1</sup> and Stéphane Deny<sup>1,2</sup>

<sup>1</sup>Department of Computer Science, Aalto University

<sup>2</sup>Department of Neuroscience and Biomedical Engineering, Aalto University  
andrea.perin@aalto.fi, stephane.deny@aalto.fi

Date: December 17, 2024

## Abstract.

Symmetries (transformations by group actions) are present in many datasets, and leveraging them holds significant promise for improving predictions in machine learning. In this work, we aim to understand when and how deep networks can *learn* symmetries from data. We focus on a supervised classification paradigm where data symmetries are only partially observed during training: some classes include all transformations of a cyclic group, while others include only a subset. This setup mimics real-world scenarios, such as learning object pose invariance from limited examples. We ask: can deep networks generalize symmetry invariance to the partially sampled classes?

In the infinite-width limit, where kernel analogies apply, we derive a *neural kernel theory of symmetry learning* to address this question. The group-cyclic nature of the dataset allows us to analyze the spectrum of neural kernels in the Fourier domain; here, we find a simple characterization of the generalization error as a function of the interaction between class separation (signal) and class-orbit density (noise). We observe that generalization can only be successful when the local structure of the data prevails over its non-local, symmetric, structure, in the kernel space defined by the architecture. This occurs when (1) classes are sufficiently distinct and (2) class orbits are sufficiently dense.

Our framework also applies to equivariant architectures (e.g., CNNs), and recovers their success in the special case where the architecture matches the inherent symmetry of the data (due to orbit collapse in kernel space). Empirically, our theory reproduces the generalization failure of finite-width networks (MLP, CNN, ViT) trained on partially observed versions of rotated-MNIST. We conclude that conventional networks trained with supervision lack a mechanism to learn symmetries that have not been explicitly embedded in their architecture *a priori*. In the future, our framework could be extended to guide the design of architectures and training procedures able to learn symmetries from data.

All code is available at <https://github.com/Andrea-Perin/gpsymm>.

## 1 Introduction

The ability to make accurate predictions depends on how well one understands the structure of a problem. Physics, notably, has achieved remarkable success in predicting natural phenomena by capturing their structure in compact mathematical equations. A key aspect of this structure lies in the concept of symmetries (Gross, 1996; Noether, 1918), which can be defined as transformations by group actions that do not change the identity of objects. For example, a chair remains a chair whether it is presented upright or upside down (a transformation in  $SO(3)$ ). In the context of deep learning, which is nowadays widely used for prediction tasks—such as identifying objects in images—a crucial question is whether deep networks have mechanisms to recognize and exploit data symmetries for effective predictions. For example, can deep networks learn to predict the identity of objects independently of their viewpoint? And importantly, do they need to be exposed to all object classes in all possible poses during training, or is exposure to some classes in some poses sufficient for them to capture the concept of pose invariance?

The field of geometric deep learning develops theories and methods that enable neural networks to take advantage of problem symmetries (Bronstein et al., 2021). In particular, equivariant neural networks (Cohen and Welling, 2016) can ensure representation equivariance and classification invariance to prespecified symmetries. However, equivariant architectures require one to know the symmetry of the problem in advance. Here, we aim to understand whether conventional deep networks, which have not been explicitly designed to capture a prespecified symmetry, can *learn symmetries directly from data*.

We focus on a supervised classification paradigm where the symmetries of the data are only partially observed during training: for some classes, all possible transformations of a cyclic group are observed during training, while for other classes only a subset of transformations is observed. This scenario mimics

realistic real-world learning problems. For example, a child sees during their development a few objects in all possible 3D poses (e.g., the toys they can manipulate), and many objects in only some poses (e.g., heavy furniture). We study whether a deep network trained on such a data diet should be expected to generalize to the partially sampled classes (e.g., recognize a piece of furniture seen from an unusual viewpoint). Specifically, we ask: under what condition(s) will the network correctly extrapolate the symmetry invariance to the partially sampled classes?

To characterize the generalization capabilities of deep networks in the presence of data symmetries, we rely on the equivalence between infinitely wide neural networks and kernel machines (Jacot et al., 2018; Lee et al., 2018; Neal, 1996a,b). Typical neural kernels (MLP, CNN) greatly simplify when computed over a dataset generated by a cyclic group action (they become circulant), allowing an interpretable analysis in the Fourier domain of when and how symmetries are correctly learned. *We find that the generalization behavior of networks is predicted by a simple ratio of inverse kernel frequency powers computed over orbits of the cyclic group.* Our analysis of this formula makes clear that deep networks (as described by their kernel equivalent) are *a priori* unable to leverage data symmetries for generalization. Successful generalization is yet possible, in cases where the local structure of the data prevails over symmetry considerations. This happens in particular (1) when classes are sufficiently well separated in kernel space, and (2) when the symmetric structure of the data is sufficiently local in kernel space. Finally, while there is no guaranteed equivalence between finite-width networks and their infinite-width counterpart, our spectral kernel theory captures well the behavior of trained networks on symmetric datasets in all our experiments.

**Outline.** We first briefly review prior theoretical work and practical methods developed for deep learning in relation to symmetries (Section 2). We then illustrate a simple symmetry learning problem, where deep networks with common architectures (MLP, CNN, ViT) are trained and evaluated on partial views of rotated-MNIST, a version of the well-known handwritten character dataset (Lecun et al., 1998) augmented with rotations (Section 3). We then analyze theoretically how kernel machines in general—and neural networks in particular—behave on datasets presenting symmetries. We build our theory through scenarios of increasing complexity, from a simple Gaussian kernel applied to a circular dataset, to deep neural kernels with or without equivariant architectures (MLPs and CNNs) applied to rotated-MNIST. In all cases, we show both theoretically and empirically the inadequacy of conventional neural architectures trained with supervision to learn symmetries that have not been embedded in their kernel design *a priori*. Our work provides theoretical tools which could prove helpful in identifying and discovering architectures and training procedures able to learn symmetries from data (as discussed in Section 4).

## 2 Prior work on deep learning, symmetries, and kernel machines

The interplay between deep learning and symmetries has been studied extensively, both empirically and theoretically, for finite-width networks and in the infinite-width limit (where kernel analogies apply). Here we attempt a condensed review of these efforts. In the following, our operational definition of *dataset symmetries* is a set of transformations by group actions that do not change the class identity of objects present in a dataset. These group transformations may act directly in the native space of the dataset (e.g., image translations) or in a latent space affecting the dataset (e.g., images of 3D-rotating objects).

**Empirically, the inability of conventional neural networks to capture symmetries present in datasets has been observed** in many different contexts. Conventional networks have been shown to fail to extrapolate a simple periodic function (Ziyin et al., 2020). In vision, studies have investigated the generalization capabilities of deep networks to recognize objects undergoing changes in pose (Abbas and Deny, 2023; Alcorn et al., 2019; Madan et al., 2022; Siddiqui et al., 2023), size (Ibrahim et al., 2022b), mirror symmetry (Sundaram et al., 2021), lighting conditions (Madan et al., 2021), and shown a substantial degradation of network performance in these conditions. Ollikka et al. (2024) showed in a recent study that humans beat state-of-the-art deep networks and most vision-language models at recognizing objects in unusual poses. In language, compositional generalization has also been framed as capturing permutation symmetries, and traditional language models have been shown to fail to capture this symmetry (Gordon et al., 2019). *In our work, we study from a theoretical point of view why networks fail to generalize on data symmetries despite being exposed to them partially during training, by characterizing network behavior on symmetric datasets in the kernel limit.*

**Network architectures have been designed to be equivariant to prespecified symmetries** (Cohen et al., 2019, 2018; Gens and Domingos, 2014; Worrall et al., 2017), or conserve certain physical quantities (Cranmer et al., 2020; Finzi et al., 2020; Greydanus et al., 2019). Network architectures have also been designed to respect the topology of a problem (for a review: Hajj et al., 2023). Relaxed and adaptive equivariance schemes have also been proposed (d’Ascoli et al., 2021; Elsayed et al., 2020; Kaba and Ravanbakhsh, 2023; Wang et al., 2022; Yeh et al., 2022; Zhou et al., 2021). The failure of traditional convolutional architectures to be fully equivariant has been observed (e.g., Azulay and Weiss, 2019), and some measure of approximate equivariance proposed (Gruver et al., 2023). Others have investigated how equivariant representations affect the capacity of group-invariant linear readouts (Farrell et al., 2021). Beyond equivariance, symmetries inherent to the architecture of deep networks have also been studied, and shown to affect their learning dynamics and solutions (Ainsworth et al., 2022; Simsek et al., 2021; Tanaka and Kunin, 2021).

**The effects of training networks on symmetry-augmented versions of a dataset have also been scrutinized.** The efficiency of training networks on augmented data vs. enforcing equivariance in the architecture has been carefully characterized at scale (Brehmer et al., 2024). Moskalev et al. (2023) clarify that training on augmented datasets does not produce genuine equivariance, in the sense that the trained networks may not be equivariant outside the training distribution. Recent theoretical results show, however, that training on a perfectly augmented dataset produces emergent equivariant representations in *ensembles* of networks, in and outside the training set, both in the finite (Nordenfors and Flinth, 2024) and infinite-width limit (Gerken and Kessel, 2024). *In our work we ask a related but different question: we study the generalization capabilities of networks trained on a dataset containing unknown symmetries—where no systematic augmentation scheme or equivariant architecture has been enforced. The symmetries in the training dataset may be well represented for some classes, but not others. The question we ask is then: how well can networks generalize the symmetry invariance to these partially sampled classes?*

Beyond equivariant and augmentation methods to deal with prespecified symmetries, **approaches to learning the symmetries present in data have been proposed** (Connor et al., 2024; Connor and Rozell, 2020; Culpepper and Olshausen, 2009; Dupont et al., 2020; Jaderberg et al., 2015; Keller and Welling, 2021a; Sanborn et al., 2023; Sohl-Dickstein et al., 2010; Zhou et al., 2021) and studied theoretically (Anselmi et al., 2019, 2023; Pfau et al., 2020). Self-supervised learning approaches build invariance (Chen et al., 2020; Ibrahim et al., 2022a; Zbontar et al., 2021; Zemel and Hinton, 1990) or equivariance (Garrido et al., 2024) to predefined symmetries by feeding augmentations of the dataset to two identical versions of the network and matching their latent representations. Disentanglement has also been framed as the problem of learning symmetries from data (Higgins et al., 2018; Mercatali et al., 2022). Subsequent work has shown, however, that topological defects result from attempting to learn disentangled representations of even the simplest symmetries such as affine transformations (Bouchacourt et al., 2021).

Beyond symmetries, **the interplay between machine learning and data geometry has been studied** for many types of data structure: compositional (Liang et al., 2024; Lippl and Stachenfeld, 2024; Sabour et al., 2017; Schott et al., 2021; Wiedemer et al., 2024), hierarchical (Mel and Ganguli, 2021; Saxe et al., 2019), data lying on a manifold (Gerace et al., 2022; Goldt et al., 2020) or on separate manifolds (Chung et al., 2018; Cohen et al., 2020; Sorscher et al., 2022).

**Two main kernel theories of deep learning exist, which identify deep networks with kernel machines** (Jacot et al., 2018; Neal, 1996a,b)<sup>1</sup>. Both theories apply in the limit where the networks have infinite width (infinite number of neurons within a layer or within a channel for convolutional networks), and both identify training a network with doing simple Gaussian Process regression over a fixed kernel determined by the network architecture. The Neural Network Gaussian Process (NNGP) theory (Neal, 1996a,b) characterizes the distribution of functions produced by random draws of the network parameters (its weights and biases), assuming a distribution from which the parameters are drawn (typically i.i.d. Normal). Conditioned on a training set, the NNGP characterizes the distribution of solutions (i.e., functions passing through the training input-label pairs) under the assumed distribution of parameters, and can be used to make predictions on a testing set. The Neural Tangent Kernel theory (NTK) (Jacot et al., 2018) describes the distribution of solutions obtained by training all layers with gradient descent, from random initial conditions. It is allegedly the most realistic theory (although see Avidan et al. (2023) for a more

<sup>1</sup>We refer the reader unfamiliar with neural kernel theories to the excellent lecture notes of Pr. Adityanarayanan Radhakrishnan available online on this topic (<https://aditradha.com/lecture-notes/>).

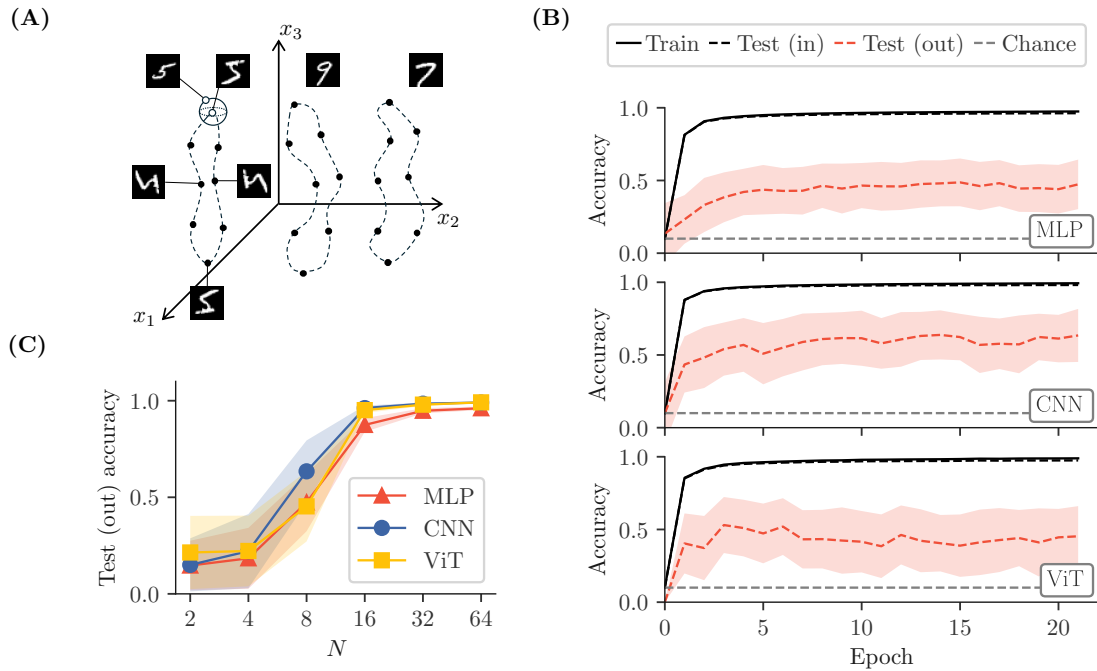


**Figure 1. Common deep network architectures fail to extrapolate symmetries from a partially observed version of rotated-MNIST.** **A:** A conceptual sketch of the learning task. For samples in the leave-out class (digit “5” in this example), the upright pose is not included in the training set (white circles). For samples in the remaining classes, all poses are included in the training set (black circles). A model that can generalize rotations should classify the missing upright samples correctly. **B:** The accuracies of the three models tested respectively on the training, *in-test* set (normal i.i.d. test set) and *out-test* set (i.e., left-out pose of the leave-out class). Chance levels (10%) are also reported as a baseline. Error shades represent 95% confidence intervals computed over all tested leave-out classes ( $n = 10$ ). **C:** Out-test accuracy for the three models as a function of the number of angles in the rotation orbit. Error shades as in **B**.

nanced account) and the one we use in this work. Nonetheless, we repeated our analyses using the NNGP kernel instead of the NTK and it did not change our conclusions (not shown). Neural kernel theories assume networks to have infinite width, which is a big approximation in practice. For example, Fort et al. (2020) show that the kernel of finite-width networks changes rapidly during the first few epochs of training to a more favourable kernel for the task, breaking the frozen kernel assumption which is only provable in the infinite-width limit. *However, in all our experiments, we find that kernel theories adequately capture the generalization behavior of finite-width trained networks on datasets presenting symmetries.*

Finally, in an insightful line of work, Bordelon et al. (2020); Canatar et al. (2021) **relate generalization properties of infinite-width deep networks to spectral properties of their kernel**. They do not however explore the specific interplay between spectral kernel properties and data symmetries. *In our work, we find that the symmetric nature of the dataset considerably simplifies the spectral description of neural kernels, allowing better interpretability of the factors on which generalization depends.*

### 3 Learning from partially observed symmetries

We start with a simple empirical study which illustrates the problem of symmetry learning and highlights the failure of a range of common architectures on this problem.

#### 3.1 Illustration of a symmetry learning problem

To illustrate the problem of symmetry learning, we train a range of networks with different architectures (MLP, ConvNet, ViT-S (Dosovitskiy, 2020)) on partially observed versions of rotated-MNIST (details of the architectures in App. B).



We start by constructing the rotated-MNIST dataset: for all samples in MNIST, we generate  $N$  rotated samples, where the rotation angles are multiples of  $2\pi/N$ . We choose a digit class, which we refer to as the *leave-out class* (Fig. 1A). We define the “training” and the “in-test” splits as a 90/10 random split of the whole rotated MNIST dataset, *except* the upright samples of the leave-out class. These samples, instead, constitute what we call the “out-test” split. *Note that predicting the labels of the out-test split is an out-of-distribution (OOD) generalization task. In this work, we study whether networks are able to perform this OOD task in virtue of the symmetric nature of the dataset.*

We report the accuracies of the three models in the case of 8 rotation angles in Fig. 1B. The in-test accuracy closely tracks the training set accuracy; however, the out-test accuracy is considerably lower for all the considered models. Training for very long times ( $>1000$  epochs) did not improve out-test accuracy (no grokking happens).

We next show that increasing the number of angles leads to better out-test performance across models (Fig. 1C). Successful generalization is achieved when the number of angles sampled is sufficiently large.

In the following, we build a theoretical framework to understand and predict the generalization abilities of deep networks on problems of this type, involving learning from partially observed symmetries. Fully developed, our theory gives a precise account of the generalization behavior of normally trained networks on rotated-MNIST observed here (Section 3.4 and Fig. 6).

### 3.2 A simple case study: Gaussian kernel regression on a circular dataset

As a first step toward our goal, we study a simple scenario which captures the relevant phenomenology for understanding the behavior of deep networks on datasets with symmetries.

**Circular dataset.** Consider the following dataset of  $2N$  points:

$$\mathcal{D} = \{(g^i \cdot x^A, +1)\}_{i=0}^{N-1} \cup \{(g^i \cdot x^B, -1)\}_{i=0}^{N-1} \subset \mathbb{R}^n \times \mathbb{R}, \quad (1)$$

where  $g$  is the representation of the generator of the cyclic group of order  $N$ , acting on  $\mathbb{R}^n$  by usual matrix multiplication. Such dataset is composed of two orbits of the same group, obtained for two different “seed” samples,  $x^A$  and  $x^B$ , which are labeled  $+1$  and  $-1$  respectively. In the following, we will use this type of dataset as a blueprint, and specialize it to different case studies. For reasons that will become apparent soon, we *order* the dataset so that points labeled  $+1$  are interleaved with those labeled  $-1$ , while preserving individual orbit ordering. For notational convenience, we denote  $x_i^\bullet = g^i \cdot x^\bullet$ . The ordered dataset can be written:

$$\mathcal{D}_o = \{(g^0 \cdot x^A, +1), (g^0 \cdot x^B, -1), (g^1 \cdot x^A, +1), \dots, (g^{N-1} \cdot x^B, -1)\} \quad (2)$$

$$= \{(x_0^A, +1), (x_0^B, -1), (x_1^A, +1), \dots, (x_{N-1}^B, -1)\}. \quad (3)$$

In this section, we begin with a simple, low dimensional instantiation of the dataset  $\mathcal{D}_o$ , where the two orbits are discretely sampled and interleaved circles of radius 1, separated by a distance  $\Delta$  (see Fig. 2A for an illustration). The following definitions of  $g$ ,  $x^A$  and  $x^B$  are thus only valid in the context of this section (Section 3.2). We consider the following  $\mathbb{R}^3$  representation of the generator  $g$ :

$$g = \begin{bmatrix} 1 & 0 & 0 \\ 0 & \cos \theta & -\sin \theta \\ 0 & \sin \theta & \cos \theta \end{bmatrix}, \quad (4)$$

where we define  $\theta = 2\pi/N$ . We consider also the seed points

$$x^A = \frac{\Delta}{2} \begin{bmatrix} 1 \\ 0 \\ 0 \end{bmatrix} + \begin{bmatrix} 0 \\ 1 \\ 0 \end{bmatrix}, \quad x^B = -\frac{\Delta}{2} \begin{bmatrix} 1 \\ 0 \\ 0 \end{bmatrix} + \begin{bmatrix} 0 \\ \cos(\theta/2) \\ \sin(\theta/2) \end{bmatrix}, \quad (5)$$

over which we make  $g$  act by usual matrix multiplication. Successive applications of  $g$  onto the seed points generate the dataset. The second seed point  $x^B$  is chosen such that the two orbits are geometrically interleaved.

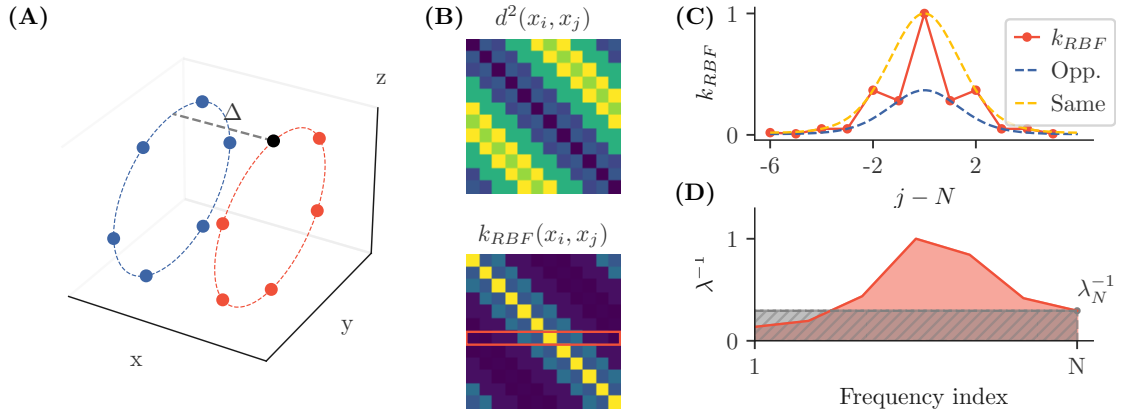


**Figure 2. Case study: Analysis of the generalization behavior of the Gaussian kernel on a circular-symmetric dataset.** **A:** A circular dataset is made of two sets of interleaved points in  $\mathbb{R}^3$  belonging to two classes (denoted in red and blue). One point (in black) is left out during training, and we regress on it. **B:** The pairwise distance matrix between the points is circulant (above), leading to a circulant kernel matrix (below) obtained by applying the Gaussian (RBF) kernel function to it elementwise. We select the  $N$ -th row from it, highlighted by the red rectangle; due to the circularity of the matrix, this comes without loss of information. **C:** A plot of the selected row of the kernel matrix. The values of the kernel alternate between two limiting curves, representing respectively the “same label” and the “opposite label” kernel values. This alternation, due to the separation between classes, is akin to the presence of a high frequency component in the kernel function itself, were it computed over the classes perfectly interleaved ( $\Delta = 0$ ). **D:** The prediction error of a Gaussian kernel on a missing point of a circular-symmetric dataset is a simple function of its spectrum (Eq. 7). The reciprocal (inverse) of the positive half of the DFT of the selected row of the kernel matrix is shown. The grey area corresponds to the numerator of the spectral error, while the red area corresponds to the denominator. The ratio of the two corresponds to the prediction error incurred by GP regression using the chosen kernel. The presence of the aforementioned high frequency component in the kernel is manifested in the low value of  $\lambda_N^{-1}$ , leading to small error (i.e., increased class separability).

**Gaussian kernel regression on a circular dataset.** We consider the following regression problem: remove any one point from the dataset  $\mathcal{D}_o$ , and find a predictor to estimate the value of  $y$  at the missing point. We solve this regression problem using *Gaussian process (GP) regression*. We select the *Gaussian or Radial Basis Function (RBF) kernel*,

$$k_{RBF}(x_i, x_j) = \exp(-L^2 \|x_i - x_j\|_2^2), \quad (6)$$

where  $L$  denotes the kernel’s length scale. We use this kernel function to compute the kernel matrix (or Gram matrix) of our dataset,  $K_{train} \in \mathbb{R}^{(2N-1) \times (2N-1)}$ . The dataset is constructed and ordered in such a way that the pairwise distance matrix computed over points of the dataset is *circulant* (Fig. 2B). The reader can convince themselves of this by noticing that the pairwise distances between points  $x_i$  and  $x_j$  in the circular orbits are only function of their absolute index difference  $|i - j|$ . Consequently, the Gaussian kernel, which is a *stationary kernel* (i.e., a kernel that only depends on the Euclidean distance between pairs of input points), also produces a *circulant* kernel matrix over the dataset. The kernel matrix is thus fully characterized by its frequency content in the Fourier domain (a circulant matrix becomes diagonal in the Fourier basis). This affords us a geometric interpretation of the generalization behavior of the kernel in the spectral (Fourier) domain.

We derive in appendix A the following equation for the prediction error  $\varepsilon_s$  of the GP on a missing point in one orbit, which we refer to in the following as the *spectral error*:

$$\varepsilon_s = \frac{\lambda_N^{-1}}{\langle \lambda^{-1} \rangle}, \quad (7)$$

where  $\lambda \in \mathbb{R}_+^{2N}$  is the spectrum of the kernel matrix  $K_{\mathcal{D}_o} \in \mathbb{R}^{2N \times 2N}$ , and  $\langle \cdot \rangle$  denotes an average over all frequencies (from  $-N$  to  $N$ ). This equation gives the prediction error of the maximum a posteriori at the missing point. Recalling that a circulant matrix is diagonalized by the *Discrete Fourier Transform* (DFT) matrix, the spectrum  $\lambda$  that is used in Eq. 7 is ordered according to increasing frequencies, so that  $\lambda_N$  is

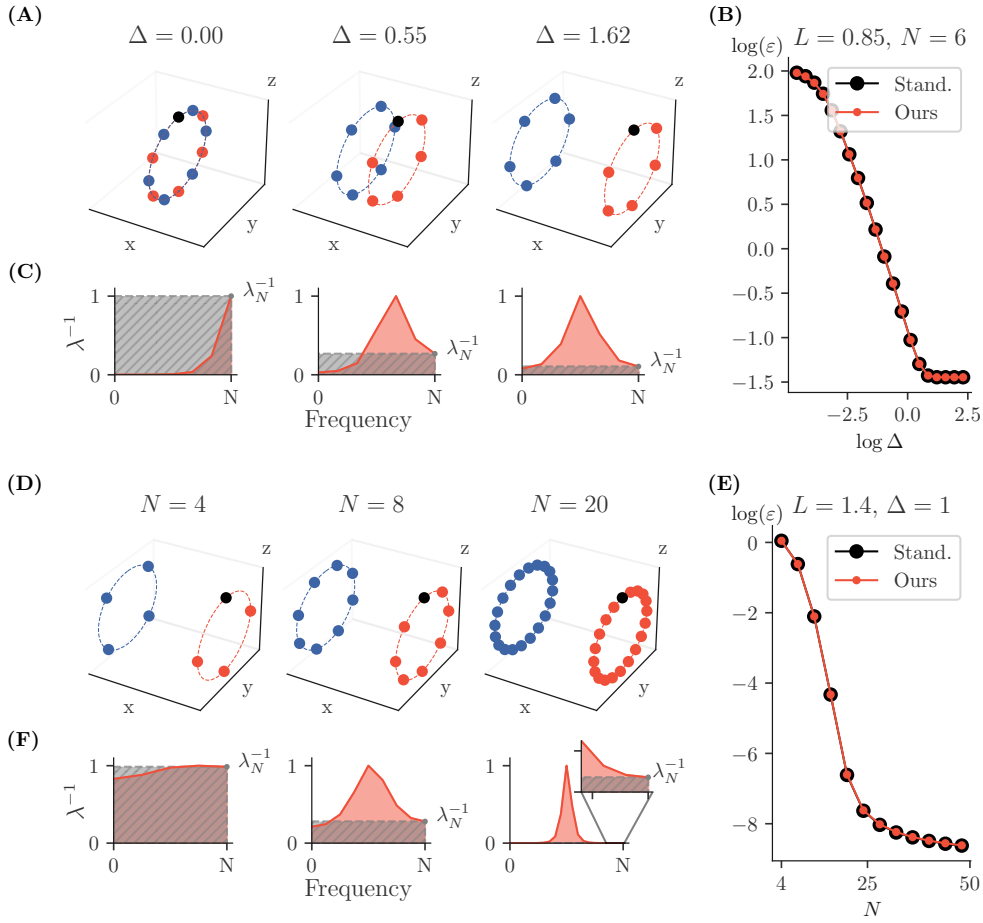


**Figure 3. Further geometric interpretations of the Gaussian kernel generalization behavior on a circular-symmetric dataset.** **A:** We progressively increase the separation  $\Delta$  between two circular classes of points (respectively in blue and red). The leave-out point used for testing is in black. **B:** The prediction error (in black) of the RBF kernel on the leave-out point decreases as a function of  $\Delta$ , as predicted by our formula (in red) given in Eq. 7 relating generalization error to spectral quantities of the kernel. **C:** Inverse spectra of the kernel matrix for different  $\Delta$ . The grey (respectively, red) area corresponds to the numerator (resp., denominator) of Eq. 7. As  $\Delta$  increases, the ratio between the grey and the red areas progressively decreases as a consequence of the last frequencies getting larger. **D, E, F:** Same as **A, B, C** where instead of increasing  $\Delta$  we increase the number of points forming each class. We see that the ratio between grey and red areas (i.e., the spectral error) progressively decreases with number of points, as a consequence of the middle inverse frequencies progressively diverging as point density increases.

the eigenvalue that corresponds to the *highest frequency*. We note that this formula can be easily extended to multiple missing points (see App. A.1).

**Geometric interpretation.** The formula of the spectral error lends itself to a simple geometric interpretation (Fig. 2C,D). Consider the spectrum obtained by applying the DFT to any one row of the kernel matrix.<sup>2</sup> We plot the inverse spectrum  $\lambda^{-1}$ . In this picture, the ratio in Eq. 7 corresponds to a ratio between areas, respectively those of a rectangle with height  $\lambda_N^{-1}$  for the numerator, and the area under the  $\lambda^{-1}$  curve for the denominator.

We now turn to two case studies, in which we present further geometrical interpretations of the spectral formula (Eq. 7), which will prove useful to understand the generalization behavior of deep networks on symmetric datasets.

<sup>2</sup>Such row is composed entirely of real entries. As a consequence, the spectrum is symmetric; we thus only show the positive half of the spectrum in the figure depictions, ranging from 0 to  $N - 1$ .

**Effect of varying  $\Delta$ .** We study the impact of the distance between orbits,  $\Delta$ , on the prediction error (Fig. 3A). We consider the dataset  $\mathcal{D}_o$  and vary  $\Delta$ , as we keep the number of points in one orbit,  $N$ , and the kernel’s length scale,  $L$ , fixed. We compute the prediction error by solving the GP regression for varying  $\Delta$ , and compare it with our formula for the spectral error (Fig. 3B). As expected by their mathematical equivalence, the two agree across the investigated range of values, and decrease as a function of  $\Delta$ . This decrease aligns with the following intuition: pulling the classes apart makes prediction over the missing point by a local kernel easier.

In Fig. 3C, we show the geometric interpretation of our spectral error. Increasing  $\Delta$ , by increasing the power of the highest frequency of the kernel matrix, skews the ratio in favor of the denominator in Eq. 7 (denoted by the red area). For  $\Delta = 0$ , the points are interleaved in the  $yz$  plane, and a kernel that would successfully generalize on the missing point would need to be dominated by its highest frequency (oscillating) component. This is not the case for the RBF kernel, whose spectrum is instead dominated by the low frequency components due to its local nature. As  $\Delta$  increases, however, the kernel’s spectrum effectively gains power in the highest frequency component, thus “aligning” its properties to the requirements imposed by the regression problem.

In summary, an increase in the distance between orbits  $\Delta$  leads to an increase in the power of the highest frequency term  $\lambda_N$  of the kernel matrix, which leads in turn to better kernel generalization on the missing point. This insight will prove useful in interpreting the generalization capabilities of a deep network on a high dimensional dataset possessing symmetries.

**Effect of varying orbit density.** We next study the impact of the number of angles,  $N$ , in an orbit on the prediction error (Fig. 3C). We compute the prediction error by solving GP regression for varying  $N$ , and compare it with our formula for the spectral error (Fig. 3D). As expected by their mathematical equivalence, the two agree across the investigated range of values, and decrease as a function of  $N$ . This decrease aligns with the following intuition: increasing the point density of an orbit makes prediction over a missing point easier.

In Fig. 3F, we show the geometric interpretation of the spectral error. Increasing  $N$  skews the ratio in favor of the denominator of Eq. 7 (denoted by the red area). The DFT projects an  $n$  dimensional signal over  $n$  discrete frequencies. For a local kernel, such as the RBF, which has most of its power slotted onto its first few low frequencies, sampling more points and then taking the DFT effectively means expanding the number of frequencies with low power, leading to the corresponding spectrum elements becoming vanishingly small. This in turn causes the average of the inverse spectrum to diverge, making the denominator of Eq. 7 grow. We note, however, that the presence of a nonzero  $\Delta$  implies that the *highest* frequency terms in general, and  $\lambda_N$  in particular, remain large, leading to the “explosion in the middle” of the inverse spectrum, which keeps the numerator in Eq. 7 small.

In summary, we see that increasing the number of angles along an orbit  $N$  leads to an increase in the average inverse spectrum  $\langle \lambda^{-1} \rangle$  (denominator of Eq. 7), and thus to a decrease in generalization error on the missing point. Again, this insight will prove useful in interpreting the generalization capabilities of a deep network on a high dimensional dataset possessing symmetries.

### 3.3 Multi-layer perceptrons (MLP) on rotated MNIST

Building on the insights from the previous section, we now turn to a more realistic setting. We study the predictions of a MLP in the Neural Tangent Kernel (NTK) limit on partial views of rotated-MNIST, a high-dimensional dataset containing a rotational symmetry.

**Datasets and architectures.** We consider the MNIST dataset, and we augment it by means of (discrete) rotations. More precisely, for each MNIST digit,  $N$  images are generated by rotation in increments of  $2\pi/N$ , capturing the full rotational range. This way, we have access to a complete *rotational orbit* for each sample. This rotation transformation corresponds, up to pixel discretization effects, to the action of a particular representation  $g$  of the cyclic group of order  $N$  (specifically, the regular representation), acting on the vector space  $\mathbb{R}^{28 \times 28}$  in which the greyscale MNIST images live. Finally, we normalize the digits to be on the sphere, making their orbits comparable with each other.

We then form *pairs* of these orbits, each pair consisting of digits from different classes. Given these datasets, we define a regression problem by leaving out one of the points in the two orbits, and asking

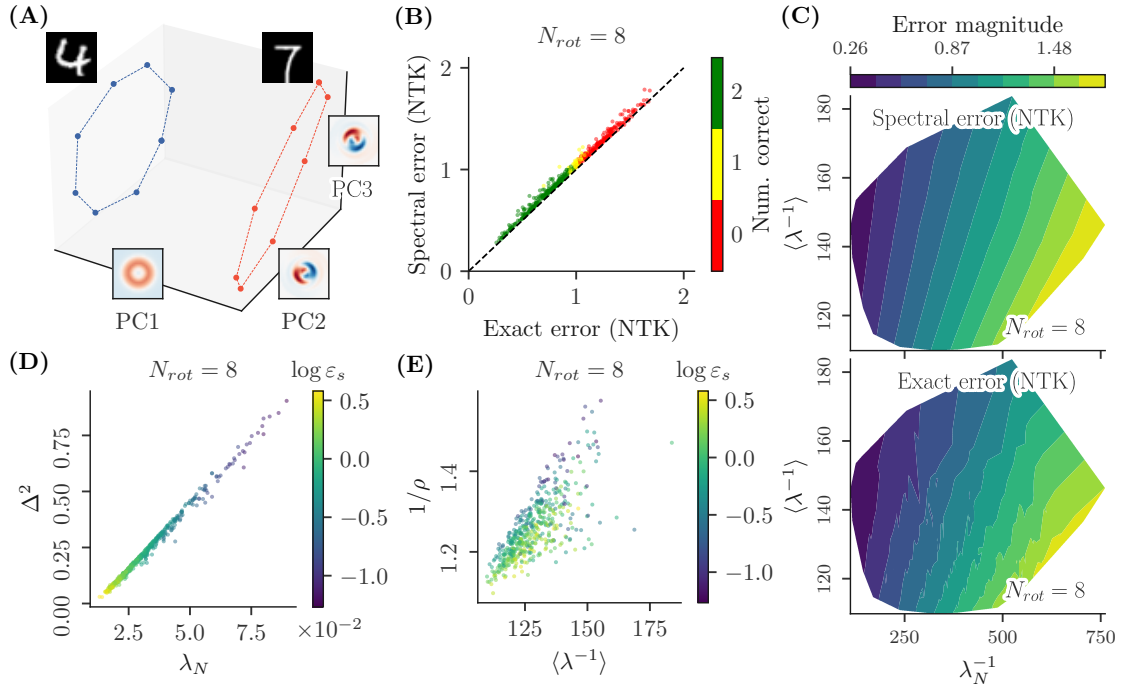


**Figure 4. Analysis of the prediction behavior of a MLP on pairs of orbits from rotated-MNIST.** **A:** We take samples of two different MNIST digits and generate their rotation orbits. The task is to predict the label value of a leave-out point in one of the two orbits. We use angle steps of 45 degrees, amounting to  $N_{rot} = 8$ . We show the points in a reduced-dimensional space obtained by performing PCA on the dataset. **B:** Scatter plot of the NTK error computed in the standard way (exact) against our spectral error (Eq. 7). Each dot corresponds to a different dataset, obtained by randomly picking pairs of digits of different classes. The line of equality is superimposed as a reference. The color coding corresponds to the number of classification errors incurred by the symmetrized NTK regression, obtained by excluding a point from class A, then from class B, and counting the number of classification errors (0, 1 or 2), understood as a disagreement in sign between NTK prediction and label of the missing point. **C:** Comparison between the spectral and exact NTK error across different values of  $\lambda_N^{-1}$  and  $\langle \lambda^{-1} \rangle$ . **D:** Comparison between the values of  $\lambda_N$  and  $\Delta^2$ . The former is the highest frequency component of the neural kernel matrix (inverse of the numerator in Eq. 7), while the latter is the distance in pixel space between the averages (centroids) of the two orbits. **E:** Comparison between the values of  $\langle \lambda^{-1} \rangle$  and  $1/\rho$ . The former is the average frequency component of the neural kernel matrix (denominator in Eq. 7), while  $\rho$  is obtained by taking the distance of each sample in both orbits from their respective centroid, and averaging them. This quantity can be interpreted as a sort of “average density” of the two involved orbits.

to find a predictor for this missing sample. Note that unlike in the more realistic scenario presented in Fig. 1, our *classes* here are constructed from a single seed sample and their orbit, and we only consider two classes. However, we show in Section 3.4 that our conclusions on this simplified setup also apply to the multi-seed-per-class and multi-class problems, with some further approximations.

We now focus on neural networks as our predictors. Specifically, we consider respectively a 1-hidden-layer and a 5-hidden-layer MLPs with ReLU activations (see App. B for more details on the architectures) in the NTK limit. In this limit, the predictions of the networks can be written as the result of Gaussian Process regression, where the kernel function is determined by the architecture of the network. Therefore, we can replicate the analysis performed in the previous section, where we replace the simple Gaussian kernel with a neural kernel. In the following, we refer to our kernel function as  $k_{NTK}$ , and the respective kernel matrix as  $K^{NTK}$ . In practice, we use the `neural-tangents` library (Novak et al., 2020) to compute the neural kernels.

Importantly, while this setup is partly analogous to the case study of the previous section (RBF kernel over a circular dataset), there are some key assumptions and approximations that need to be justified before we can apply the theory to this case.



**Assumption 1: Circularity of the kernel matrix over one orbit.** Firstly, the NTK of a MLP is a *dot product* kernel. As a consequence, it is not *stationary* (it is not solely function of the Euclidean distance between pairs of input points); instead, it is a function of the angle between the two input vectors (Neal, 1996b). However, in virtue of the simple cyclic nature of our datasets, the kernel matrix  $K_{ij} = k(x_i, x_j)$  corresponding to the kernel function induced by the MLP *on a single class* is circulant.

*Proof.* Consider class A. The cyclic group acts on points of class A linearly via its (matrix) representation  $R$ ; due to the properties of the cyclic group, such representation is orthogonal. The dot product between data points thus only depends on their index difference, as indexed by the group action:

$$(x_i^A)^T x_j^A = (R^i x_0^A)^T (R^j x_0^A) = (x_0^A)^T R^{-i} R^j x_0^A = (x_0^A)^T R^{j-i} x_0^A \quad (8)$$

As the kernel of a MLP only depends on the scalar product of its inputs, it thus also only depends on the index distance between the data points:

$$K_{ij} = k(x_i^A, x_j^A) = k((x_i^A)^T x_j^A) = k((x_0^A)^T R^{j-i} x_0^A), \quad (9)$$

and thus the  $(i, j)$  entry of the kernel matrix depends only on the difference between the two indices  $(i - j)$ . The neural kernel computed over a single class is thus circulant.  $\square$

**Assumption 2: Circularity of the kernel matrix over the dataset made of two orbits.** Secondly, MNIST digits from different classes are in general not *geometrically* interleaved, i.e., a point in one orbit is not equidistant from the “neighboring” points in the other orbit. This can be written as the following dot product condition:

$$x_i^A \cdot x_i^B \neq x_i^A \cdot x_{i+1}^B. \quad (10)$$

Furthermore, the angular distance between first neighbors in each orbit is not necessarily the same, i.e.,

$$x_i^A \cdot x_{i+1}^A \neq x_i^B \cdot x_{i+1}^B. \quad (11)$$

Indeed, even though the seed images are all normalized to be on the sphere, the angular distance between first neighbors on an orbit still depends on how close the seed image is to the stabilizer of the group action. Take for instance a seed image with perfect central symmetry (e.g., a perfect ‘o’); all rotations of the seed image are the seed image themselves, and thus the angular distance is 0. Conversely, for a “Dirac delta”-like image (i.e., an image that is nonzero at a single point, assuming infinite pixel resolution), all rotated images are orthogonal to each other, setting their angular difference to 1. The angular distance between first neighbors on a same orbit thus sits between 0 and 1, depending on the smoothness of the image with respect to the group transformation.

As a consequence, the following NTK matrix is in general not circulant<sup>3</sup>:

$$K^{\text{NTK}} = k_{\text{NTK}} \begin{pmatrix} x_0^A \cdot x_0^A & x_0^A \cdot x_0^B & x_0^A \cdot x_1^A & x_0^A \cdot x_1^B & x_0^A \cdot x_2^A & \dots \\ x_0^B \cdot x_0^A & x_0^B \cdot x_0^B & x_0^B \cdot x_1^A & x_0^B \cdot x_1^B & x_0^B \cdot x_2^A & \dots \\ x_1^A \cdot x_0^A & x_1^A \cdot x_0^B & x_1^A \cdot x_1^A & x_1^A \cdot x_1^B & x_1^A \cdot x_2^A & \dots \\ x_1^B \cdot x_0^A & x_1^B \cdot x_0^B & x_1^B \cdot x_1^A & x_1^B \cdot x_1^B & x_1^B \cdot x_2^A & \dots \\ x_2^A \cdot x_0^A & x_2^A \cdot x_0^B & x_2^A \cdot x_1^A & x_2^A \cdot x_1^B & x_2^A \cdot x_2^A & \dots \\ \vdots & \vdots & \vdots & \vdots & \vdots & \ddots \end{pmatrix}$$

To retrieve the setup outlined in the previous section, we resort to an *ex-post* circularization procedure. We consider the matrix  $\tilde{K}^{\text{NTK}}$  that is obtained by taking the diagonal-wise average of the kernel matrix  $K^{\text{NTK}}$ :

$$\tilde{K}_{ij}^{\text{NTK}} = \frac{1}{2N} \sum_k K_{(i+k)\% (2N), (j+k)\% (2N)}^{\text{NTK}}. \quad (12)$$

<sup>3</sup>We remark, however, that the first diagonal, denoted in black, is constant in virtue of the fact that we normalize each data point to be on the sphere.

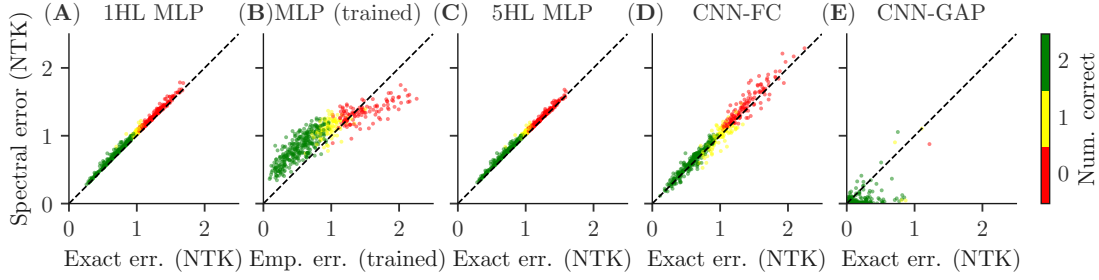


**Figure 5. Spectral error matches exact NTK error across various architectures and for finite-width networks, on rotated-MNIST orbit pairs:** (A) a MLP with 1 hidden layer, (B) a finite-width 1-hidden layer MLP trained with Adam, (C) a MLP with 5 hidden layers, (D) a ConvNet with a fully-connected last layer, (E) a ConvNet with global average pooling at the last layer. In this case, the assumptions of the theory are too crude to capture empirical phenomenology (see text). Color coding as in Fig. 4B.

Such matrix is by definition circulant. The practical meaning of this procedure is twofold: the averaging of *even* diagonals imposes that both classes’ feature embeddings are “equally spaced” along the orbit, while the averaging of *odd* diagonals (together with the intrinsic symmetry of the kernel matrix) imposes that the feature embeddings are interleaved in the sense that  $\tilde{K}_{i,i+1}^{NTK} = \tilde{K}_{i,i-1}^{NTK}$ . We stress that this circularization procedure is not justified a priori. However, we empirically show that it is a realistic approximation for analyzing the interplay between symmetric datasets and deep networks.

**Assumption 3: Symmetrization of the NTK error w.r.t. to class.** Lastly, because of the asymmetry between orbits, removal of a point from one orbit is not in general equivalent to removal of a point from the other orbit. Yet, our formula for the spectral error, operating on the circularized kernel matrix, is intrinsically symmetric. To restore this interchangeability in the standard NTK error, we consider in the following a *symmetrized NTK error*, which we obtain by averaging the NTK prediction errors that arise by removing a point from either one orbit or the other. It is this symmetrized NTK error that we compare with the spectral error.

**Results.** Equipped now with a circulant kernel matrix, we can once again refer to the spectral error formula of Eq. 7 for the estimation of the prediction error associated with performing GP regression under the kernel matrix  $\tilde{K}^{NTK}$ .

We find that the spectral error tracks the symmetrized NTK error across all sampled pairs (Fig. 4B). This agreement holds across the whole range of explored values for both  $\lambda_N$  and  $\langle \lambda^{-1} \rangle$  (Fig. 4C), and regardless of number of rotation angles (App. D). Moreover, this agreement qualitatively holds for finite-width, trained networks (Fig. 5B and App. E), as well as for deeper MLPs (Fig. 5C and App. E). This suggests that the circularization procedure preserves the overall structure of the problem, and allows us to establish a parallel to the low dimensional case study previously analyzed.

**Geometric interpretation.** We can now interpret the quantities involved in the spectral error (Eq. 7) in light of the insights we obtained in the low dimensional case. This affords us a geometric interpretation of the quantities that drive symmetry learning performance. Firstly, we can effectively read the highest frequency eigenvalue  $\lambda_N$  as a high-dimensional analogue to the orbit separation  $\Delta$  in Eq. 5. Indeed, the values of  $\lambda_N$  and the euclidean distance between orbit averages in input space are, for the explored ranges, in an approximate linear relationship (Fig. 4D). As a consequence (and perhaps tracking intuition), one can see how the separation between the orbits is a key indicator of prediction error. Secondly, we can map the average reciprocal spectrum  $\langle \lambda^{-1} \rangle$  to a measure of orbit density, computed as the *inverse of the orbit radius*<sup>4</sup>. We see that these two quantities are in an approximately linear relation (Fig. 4E). These

<sup>4</sup>The orbit radius is computed as the distance of any orbit sample to the orbit centroid, in the high-dimensional dataset space. It is a measure of how close the seed image is from the stabilizer of the group action. For example, a seed image that is rotation invariant, such as a perfect ‘o’, is situated on the stabilizer of the rotation group action, leading to a null radius. In our theory, we find that the orbit radii of two orbit-classes to separate is a determinant factor for correct generalization.

relations enable a geometric interpretation of the quantities that inform class separability, mainly the distance between classes  $\Delta$  and the density of orbit-classes. Note, however, that the observed mapping between spectral quantities of the kernel and geometric quantities in input space is empirical and not guaranteed to hold for all datasets or architectures. In particular, we show later that this equivalence breaks for a convolutional neural network with global average pooling at the last layer.

### 3.4 Extension to multiple seeds per class and multiple classes

Until now, we have only considered a simplified scenario in which the datasets are composed of a single orbit per class, and where there are only two classes. We now ask whether the theory can also be adapted to a more realistic scenario, where the datasets are composed of multiple seed images per class, and where there are multiple classes, only one of which has a missing angle during training. This setting is the one we presented at the start of this study (Fig 1). Below, we show that our framework can be extended to this scenario.

**Extension to multiple seed points per class.** First, we describe how our framework can be extended to multiple seeds per class and two classes. We make a twofold assumption: that (1) the interclass interactions can be effectively summarized by pairwise interactions between orbits of different classes, and (2) orbits belonging to the same class do not interact for the purpose of prediction.

For all pairs of seeds that can be formed across the two classes, we compute a spectral error according to Eq. 7. By doing so, we are considering the case of a missing point in either of these two orbits. We then average the error over all the pairs, obtaining a single, average spectral error.

We compare this average spectral error against the exact NTK error, computed over the entire dataset. We obtain the exact error by running NTK regression on the dataset that contains all orbits of both classes, excluding one angle from all orbits of one class. On said angles, we compute the NTK regression error, averaged over all orbits. We then compute its symmetrized version by swapping the two classes, and averaging the two error values.

We test the agreement between the pair-averaged spectral error and symmetrized NTK error across many trials, where each trial corresponds to a different dataset, obtained by taking a number of seeds ( $N_{\text{seed}} = 13$ ) from each of two different, randomly picked MNIST digit classes. We find empirically that the average spectral error correctly predicts exact NTK error across a large number of such trials (Fig. 6A, extended version in App. F).

In conclusion, our spectral theory, which simply considers the average pairwise interaction between orbits of different classes, predicts well the generalization behavior of infinite-width networks on a dataset comprising multiple seeds per class.

**Extension to multiple classes.** We now describe how our framework can be extended to the 10 classes of MNIST. We stress that, in principle, NTK regression is not suited to predict the results of a network that is trained with a cross-entropy loss on multiple classes. However, we show that we can adapt our spectral theory to this scenario, and qualitatively model the results of such training. We do so by employing a *one-versus-many* strategy.

Consider an orbit from class A. Form all pairs with orbits of another class B (there are  $N_{\text{seed}} = 13$  such pairs). Average the spectral prediction obtained from all these pairwise comparisons. Repeat this comparison with all other classes C, D, E, etc. We thus obtain a prediction for a missing point in the orbit of class A against every other *class*. If *all* of these class-wise predictions are correct, we consider the network prediction on this orbit of class A to be correct. We extend this procedure to all orbits of class A, and count the percentage of correctly classified orbits for that class. We repeat this procedure for every possible leave-out class, and report the average accuracy of our classifier over all leave-out classes.

We compare the predicted accuracy resulting from this procedure, to the empirical accuracy of a finite-width 2-hidden-layer MLP trained with Adam and a cross-entropy loss (see details of architecture in App. B.3), on a version of rotated-MNIST comprising  $N_{\text{seed}} = 13$  seeds per class (we limit the number of seeds per class to 13 because of the prohibitive computational cost of computing NTK regression on larger datasets).

The spectral accuracy qualitatively matches the empirical accuracy of the trained network as we vary the number of points composing the orbits (Fig. 6B, extended version in App. Fig. 13). The spectral

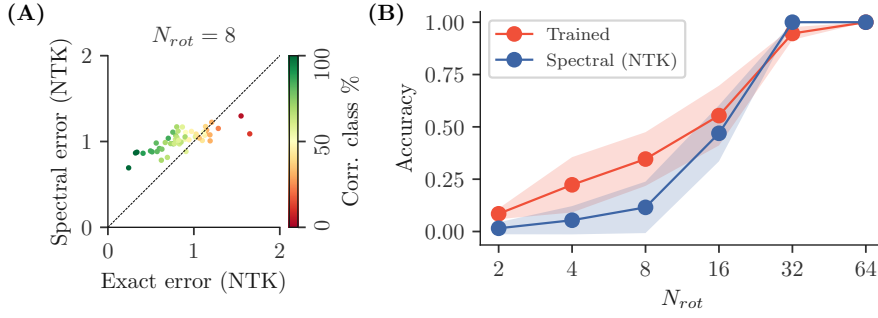


**Figure 6. Application of the spectral theory to a MLP trained on a version of rotated-MNIST comprising multiple seeds per class and multiple classes.** **A:** For datasets comprised of two classes of rotated-MNIST, comprising multiple seeds each ( $N_{\text{seed}} = 13$ ), we compare the average spectral error, obtained by averaging over all pairings of orbits in the dataset, with the symmetrized NTK prediction error, computed over all possible missing points. Each dot in the scatter plot represents a different dataset, drawn by randomly selecting two classes from MNIST, and randomly selecting 13 seed images per class. The color coding reflects the percentage of seeds (of both classes) for which the NTK regression gives a correct prediction, understood as agreeing in its sign with the label of the missing points. **B:** On a multi-class (10 classes of MNIST), multi-seed-per-class ( $N_{\text{seed}} = 13$ ) version of rotated-MNIST, we compare the generalization accuracy predicted by our multi-class adapted spectral error, with the one of a normally trained MLP (2 hidden layers, trained with a cross-entropy loss). As the number of points in the orbits increases, both trained and spectral accuracies increase on the classification task, progressively and similarly, suggesting that no mechanism for symmetry learning is present for finite-width trained networks that would be unaccounted for by the spectral theory.

accuracy curve also mirrors the empirical curves obtained by training various architectures (MLP, CNN, ViT) on a full version of rotated-MNIST at the beginning of this study (Fig. 1).

*In conclusion, our spectral theory, which only considers pairwise interactions between seeds across classes, and lends itself to a simple geometric interpretation of the factors leading to correct generalization (namely class distance and orbit density), qualitatively recapitulates the lack of generalization of conventionally trained finite-width networks on a realistic dataset, rotated-MNIST, comprising multiple classes and multiple seeds per class. This result provides strong evidence that the ability of conventional deep networks to generalize on a symmetric dataset is essentially dictated by the local geometric properties of the dataset, and that no specific mechanism allows such networks to “grok” (learn from examples) the non-local, symmetric structure of a prediction problem.*

### 3.5 Extension to equivariant architectures

We here study how the interplay between dataset symmetries and equivariant architectures affects generalization.

For simplicity and concreteness, we focus our study on spatially convolutional neural networks. We distinguish two types of convolutional architectures: (1) convolutional architectures where the last layer is fully connected: these architectures do not ensure full invariance to translation; (2) convolutional architectures where the last layer performs global average pooling, ensuring invariance to translation.

We also distinguish two cases of data symmetries: (1) when the symmetry in the data corresponds to the one encoded in the equivariant architecture; (2) when it does not, and the architecture is equivariant to another, different symmetry. We consider a dataset with translational symmetry to illustrate the first case (a convolutional neural network is equivariant to translations) and a dataset with rotational symmetry to illustrate the second case (a convolutional neural network is not equivariant to image rotations).

Through these examples, we build a framework that should be easily expandable to characterize how equivariant architectures and dataset symmetries interact in general.

Below, we provide formal definitions for the aforementioned datasets and network architectures, and then proceed to state the results.

### 3.5.1 Definitions

**Dataset with translational symmetry.** We consider a dataset composed of seed images and all their translations. For the purpose of the proofs to follow, we will focus on a single orbit of this dataset, which consists of a single seed point  $x_s \in \mathbb{R}^{n \times n}$  and all of its translations:

$$\mathcal{O}_T = \{g_T^0 \cdot x_s, g_T^1 \cdot x_s, \dots, g_T^{n-1} \cdot x_s\}, \quad (13)$$

where the translation operator  $g_T$  acts on images by circularly shifting them along one of the dimensions. For pixel coordinates  $(i_x, i_y)$ , and the corresponding value of the pixel  $x(i_x, i_y)$ , we write:

$$g_T \cdot x \left( \begin{bmatrix} i_x \\ i_y \end{bmatrix} \right) = x \left( \begin{bmatrix} (i_x + 1) \bmod n \\ i_y \end{bmatrix} \right) \quad (14)$$

**Dataset with rotational symmetry.** We consider a dataset composed of seed images and all their rotations in  $C_4$  (we limit ourselves to 4 cardinal rotations to avoid definitional problems of image rotation on discrete pixel grids). We will focus on a single orbit of this dataset, which consists in a single seed point  $x_s \in \mathbb{R}^{n \times n}$  and all its rotations:

$$\mathcal{O}_R = \{g_R^0 \cdot x_s, g_R^1 \cdot x_s, g_R^2 \cdot x_s, g_R^3 \cdot x_s\} \quad (15)$$

where the rotation operator  $g_R$  permutes pixel coordinates  $(i_x, i_y)$  as follows:

$$g_R \cdot x \left( \begin{bmatrix} i_x \\ i_y \end{bmatrix} \right) = x \left( \begin{bmatrix} i_y \\ n - i_x \end{bmatrix} \right) \quad (16)$$

**Fully connected convolutional network (FC).** We consider a fully connected convolutional network with one hidden layer, filters of size  $3 \times 3$ , circular padding and stride of 1. The network  $f : \mathbb{R}^{n \times n} \rightarrow \mathbb{R}$  is parameterized by:

$$f_{\text{FC}}(x) = A \frac{1}{\sqrt{k}} \phi(B \otimes x)_v, \quad (17)$$

where  $A \in \mathbb{R}^{1 \times n^2 k}$ ,  $B \in \mathbb{R}^{k \times 1 \times 3 \times 3}$ ,  $\otimes$  denotes the spatial convolution operation, and for any matrix  $u \in \mathbb{R}^{n \times n}$ ,  $u_v \in \mathbb{R}^{n^2}$  denotes the vectorization (i.e., flattening) of  $u$ . This network first applies a convolutional layer to the data, then flattens the resulting representation into a vector, and passes it through a fully connected layer.

**Global Average Pooling convolutional network (GAP).** We consider a convolutional network with global average pooling at the last layer. This network is invariant to discrete translations. The network  $f_{\text{GAP}} : \mathbb{R}^{n \times n} \rightarrow \mathbb{R}$  is parameterized by:

$$f_{\text{GAP}}(x) = \frac{1}{\sqrt{k}n^2} \sum_k \sum_{i_x} \sum_{i_y} A_{1k} \phi(B_{k,i_x,i_y} \cdot x) \quad (18)$$

where  $A \in \mathbb{R}^{1 \times k}$ , and  $B \in \mathbb{R}^{k \times 1 \times 3 \times 3}$  with  $B_k \in \mathbb{R}^{1 \times 1 \times 3 \times 3}$  indexing filter  $k$  of  $B$ .  $B_{k,i_x,i_y} \in \mathbb{R}^{1 \times 1 \times n \times n}$  is obtained by centering  $B_k$  at coordinates  $(i_x, i_y)$  of an  $n \times n$  grid with periodic boundary conditions, and filling the remaining entries with zeros. Then, the dot product is understood as the sum of the elementwise multiplications of all entries of  $x$  and  $B_{k,i_x,i_y}$ . We remark that this operation is effectively an alternative way of describing a convolution with filter bank  $B$ , but this indexing choice proves useful in the proofs (see App. C). After applying a convolutional layer to the data, this network averages the resulting representation across each of the  $k$  output channels, and then takes a linear combination of these averages using a fully connected layer.



### 3.5.2 Theoretical results

We showed previously that the generalization behavior of MLPs on a symmetric dataset, rotated-MNIST, is well captured by the spectral error, a quantity computed from the Fourier components of the MLP kernel over the (orbits of the) cyclic group of interest. Crucially, the derivation of this result relied on the circulant structure of the kernel matrix, which in turn was a consequence of the dot product nature of the MLP kernel.

Convolutional neural networks, however, are *not* dot product kernels, as pixel proximity plays a role in the kernel similarity between two images (Arora et al., 2019). Nevertheless, here we show that the kernel matrix of convolutional neural networks *is also circulant* over common representations of the cyclic group, regardless of whether the equivariance matches the symmetry of the data or not. We thus get that the same spectral theory of generalization applies to these equivariant architectures. Furthermore, a well-known special case arises when the network is designed to be fully invariant to the symmetry of interest, which is also well captured by our spectral theory.

First, we study the interplay between an equivariant architecture and its matching symmetry.

**Proposition 1.** *The kernel matrix of a fully connected convolutional network  $K_{FC}$  over a translation orbit  $O_T$  is circulant. Moreover, this kernel matrix is in general not constant or rank-deficient.*

See App. C for a proof of this proposition and the propositions below.

The kernel matrix of a fully connected convolutional network being circulant over a translation orbit, it can be analyzed in the Fourier domain, as done in the previous sections for a MLP. The same spectral formula for generalization error can thus be derived for this architecture and symmetry. Moreover, the kernel matrix is in general not rank-deficient the translation orbit. This implies that, *a priori*, no inverse eigenvalue will diverge in the denominator of Eq. 7. Were this to happen, the spectral error would go to 0, i.e., the network would achieve perfect generalization. The same conclusion about the inability of a MLP to extrapolate symmetries to partially observed classes thus holds for a fully connected convolutional network on a dataset with translational symmetry.

**Proposition 2.** *The kernel matrix of a global average pooling convolutional network  $K_{GAP}$  over a translation orbit  $O_T$  is constant.*

The kernel matrix of a global average pooling convolutional network is not only circulant, but also constant. The kernel matrix computed over a dataset made of two orbits of two different classes is thus blockwise-constant in 2x2 blocks, one for each orbit, and by consequence rank-deficient. This ensures that some of the eigenvalues of the kernel matrix are null, leading the denominator of the spectral error (Eq. 7) to diverge and thus perfect generalization (0 error)<sup>5</sup>. We thus recover the well-known fact that a convolutional network with global average pooling at the last layer makes predictions that are by construction invariant to translations, and thus correctly generalizes from a partial view of a class orbit.

Second, we study the interplay between an equivariant architecture and a mismatching symmetry.

**Proposition 3.** *The kernel matrix of a fully connected convolutional network  $K_{FC}$  over a rotation orbit  $O_R$  is circulant, but in general not constant or rank-deficient.*

For a fully connected convolutional network applied to a dataset with rotational symmetry, the kernel matrix over an orbit remains circulant. Therefore, the same spectral theory of generalization applies as before. The kernel matrix is in general neither constant nor rank-deficient, and thus generalization on the missing point is not guaranteed to succeed.

**Proposition 4.** *The kernel matrix of a global average pooling convolutional network  $K_{GAP}$  over a rotation orbit  $O_R$  is circulant, but in general not rank-deficient or constant.*

The implication of this last proposition is that (1) our spectral theory applies to this scenario as well, and (2) unlike for translations, the global average pooling layer does not guarantee perfect generalization on a rotation orbit.

<sup>5</sup>provided that the last frequency has non-zero power, i.e., the two classes are not fully collapsed in kernel space.

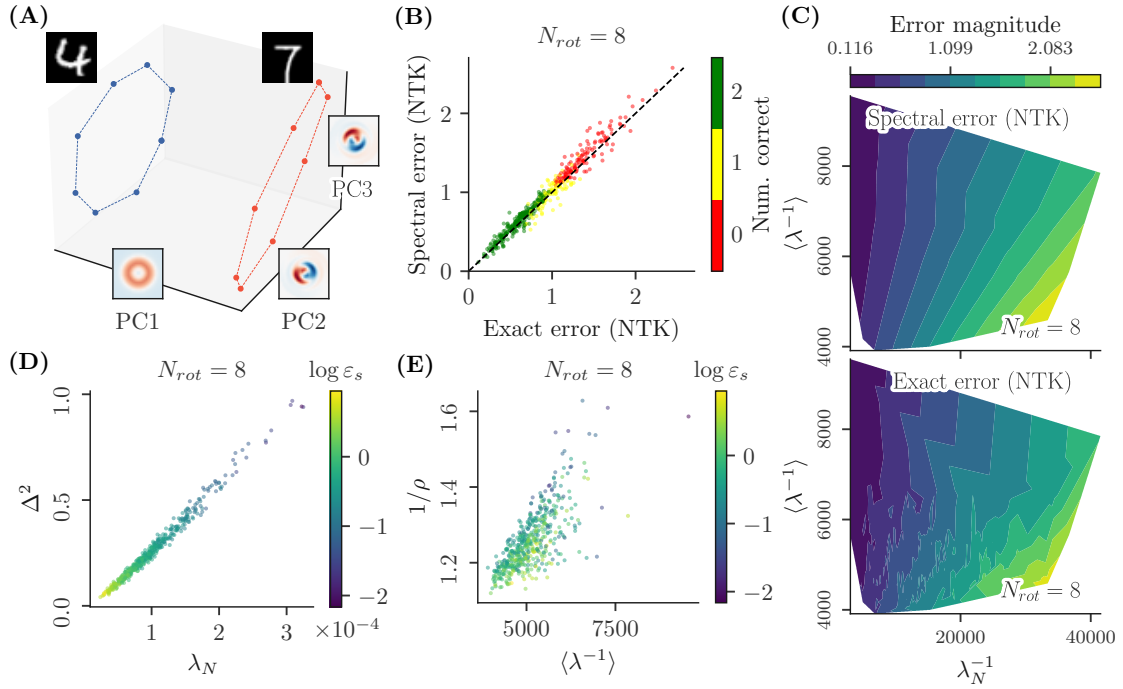


Figure 7. Analysis of the prediction behavior of a fully connected convolutional network on pairs of orbits from rotated-MNIST. Same caption as in Fig. 4.

### 3.5.3 Empirical results

Empirically, we repeat the analyses previously performed on MLPs using convolutional architectures and obtain essentially the same results.

**Fully connected (FC) convolutional network on rotated-MNIST.** We first analyze the behavior of a fully connected (FC) convolutional network, on the task of classifying a missing point from a dataset composed of two orbits, each generated from 8 rotations of a seed MNIST digit. The FC kernel matrix over a rotation orbit is circulant, as predicted by Prop. 3, allowing us to apply the spectral formula as we did for a MLP. The spectral error predicts well the symmetrized NTK error, across all pairs of orbits tested (Fig. 5C). As with a MLP, the numerator and denominator values of the spectral error are approximately proportional to the distance between classes in input space and their average orbit density respectively (Fig. 7), allowing the same interpretation of the factors that lead to successful generalization as for the MLP.

**Global average pooling (GAP) convolutional network on rotated-MNIST.** We next consider a global average pooling convolutional network, on the same task and datasets. Its kernel matrix over a rotation orbit is also circulant, as predicted by Prop. 4, allowing us to apply the spectral theory. The prediction errors are in general remarkably low (but, crucially, not 0) for this architecture on these datasets (Fig. 5D). While we lack a comprehensive theory for this success, we speculate that the GAP convolutional network finds similarities in the local structure of images belonging to the same rotation orbit, allowing it to outperform other architectures. Interestingly, we find that a GAP convolutional network architecture where the filters don't overlap (i.e., the stride matches filter size) fails to correctly classify all pairs of orbits (App. Fig. 16).

Moreover, the agreement between exact NTK error and spectral error that can be observed for other architectures is here worse, although still reasonable (both methods predict low error). Our interpretation of why spectral error is not a very good approximation of exact NTK error here, is that the post-hoc circularization of the kernel matrix may reshape its structure too drastically. For instance, the geometric interleaving between the two orbits that is assumed by the circularization, may not be a good approximation in this kernel space.

Finally, as shown in App. G.1, the numerator and denominator values of the spectral error do not map well to the distance between classes in input space and their average orbit density. *This illustrates the important fact that, for some neural architectures, the spectral quantities computed in kernel space are not direct correlates of simple geometric quantities in input space, and cannot be interpreted as simply.*

**Convolutional networks on translated-MNIST.** We next analyze the behavior of convolutional networks on pairs of orbits of translated-MNIST, a version of MNIST where the digits are translated along the image  $x$ -axis, with periodic boundary condition (App. G.2). Using a fully connected convolutional network, we do not see good generalization, as predicted by Prop. 1, and in good quantitative agreement with the spectral formula. Using a global average pooling convolutional network, we see perfect generalization of the network on the leave-out class (error is 0 to numerical precision), as expected from the fact that this architecture is invariant to translation. In our spectral formula, this perfect generalization is realized by the fact that the denominator of Eq. 7 diverges, as a consequence of the kernel matrix being rank-deficient (a consequence of Prop. 2).

## 4 Discussion

In this work we establish a theory on when, and to what extent, deep networks are capable of learning symmetries from data. We find that the generalization behavior of conventional networks trained with supervision on datasets presenting a cyclic-group symmetry is captured by a simple ratio of inverse kernel frequency powers. Our analysis of this formula sheds light on the limitations of conventional architectures trained with supervision to learn symmetries from data. In particular, we find that they are generally unable to extrapolate symmetries observed exhaustively on some classes to other partially sampled classes. Accurate generalization is only possible when the local structure of the data in kernel space (determined by network architecture) allows for correct generalization. In other words, conventional networks have no mechanism to learn symmetries that have not been embedded in their architecture *a priori* through equivariance.

This result may seem at odds with the notion that deep networks are biased to find simple solutions (Humayun et al., 2024; Ortiz-Jiménez et al., 2020; Power et al., 2022; Shah et al., 2020; Zhang et al., 2021). In our study, networks are blind to the simple symmetric structure of the data. Were they to notice this simple structure, they would achieve data-efficient generalization. However, results showing that networks have a bias towards simplicity typically define simplicity as a notion of local structure in the data. These studies show that networks find the smoothest possible function capturing the training set. Here, however, the symmetric structure of the data is not a local structure: rotated versions of a digit are not close in pixel space to the upright digit, and they may even be closer to a different digit class altogether. For example, a ‘4’ upside down might look more like a ‘6’ than like another upright ‘4’. It is thus expected that networks with a bias for smooth solutions will fail on such task, in the absence of a mechanism to detect symmetries. Networks biased to find the *shortest description* of a dataset (in the sense of Kolmogorov complexity) may perform better on this task (Valle-Perez et al., 2019), but progress in this area is limited.

On the other hand, our findings are compatible with the scaling laws observed when training deep networks (Bahri et al., 2024; Kaplan et al., 2020). Scaling laws show that deep networks continuously improve on generalization as the number of samples in the training set increases. Mapped to our setup, this corresponds to our observation that network performance gradually increases with the number of angles sampled from the group orbits. We see no abrupt change in generalization performance that would indicate that the network captures or “groks” the symmetry invariance, even with very long training times. An important implication of this observation is that networks should be data-inefficient on data presenting symmetries, as confirmed empirically by the ever-growing datasets used for training them (e.g., in computer vision JFT-300M (Sun et al., 2017), IG-3.6B (Singh et al., 2022) and LAION-5B (Schuhmann et al., 2022)). As the number of symmetric transformations present in the dataset increases (e.g., image rotation, translation, scaling, etc.), we only expect this generalization difficulty to grow, as this leads to a combinatorial explosion of possible transformations (Schott et al., 2021). This combinatorial explosion could partly be responsible for the brittleness of current deep learning approaches on edge cases, as observed for instance in Abbas and Deny (2023).

Many methods have been proposed to learn symmetries from data. For example, some propose to leverage more supervision by pairing images undergoing a symmetric transformation during training. This is the case, for instance, of self-supervised learning approaches via joint embedding (Geiping et al., 2023), and of autoencoder approaches (Connor et al., 2024; Connor and Rozell, 2020; Dupont et al., 2020; Keller and Welling, 2021b), the goal of which is to map one sample to a transformed version of itself via an autoencoder equipped with transformation operators in latent space. Empirically, these methods are found to somewhat generalize group transformations (e.g., 3D rotations) to object classes that were not seen during training. Other directions include meta-learning approaches (Finn et al., 2017; Yang and Hu, 2020), feature learning approaches (Yang et al., 2023) and dynamic architecture choices (Chauhan et al., 2024; Stanley and Miikkulainen, 2002), which could potentially alleviate the problem of having a fixed, frozen, kernel incapable of adapting to problem symmetries. Indeed, our understanding is that networks cannot learn symmetries because their kernel is defined by their architecture, and cannot adapt to the symmetries of a given dataset. Designing mechanisms to adapt the kernel induced by the network to the symmetries of the problem at stake seems a likely path forward to devise more data-efficient deep networks. In future work, we would like to extend our theory to these methods, and establish whether they are theoretically able to learn symmetries from data, and if so, to what extent.

Our theory could also be extended in various ways to capture a richer phenomenology. First, we have focused on the simple discrete one-dimensional cyclic group in this study. It would be interesting to understand whether and how the theory could be extended to continuous, high-dimensional and more complicated groups, such as  $SO(3)$ . Second, our study focuses on symmetries that are “native” to the space in which the datasets reside (e.g., image rotations). However, group actions may more realistically exist in a latent space affecting the dataset indirectly (e.g., images of 3D-rotated objects). This latter case is particularly interesting because architectures cannot easily be designed to be equivariant to symmetries which are not directly acting in dataset space. We note, however, that given the failure of conventional architectures to correctly generalize simple symmetries native to the dataset space, we do not expect these same architectures to be able to learn more complex, latent space symmetries.

A source of inspiration for learning symmetries could be found in cognitive science and neuroscience. Empirically, there is evidence that humans are superior to deep networks at some tasks necessitating symmetry invariance. Recently, Ollikka et al. (2024) show that humans beat state-of-the-art deep networks and most vision-language models at recognizing objects in unusual poses. Humans are also known to be able to reason about problem symmetries, for example in the problem of mental rotation (Shepard and Metzler, 1971). Interestingly, the time for subjects to compare one 3D object to another in mental rotation tasks is proportional to the angular difference between the two objects, implying that some recurrent processes in the brain may be involved, recurrence lacking from current state-of-the-art architectures in deep learning. There is also evidence that the mental rotation ability is learned through experience (or at least not fully operational at birth), as studies on infants show that there is a critical age when they are able to perform this task (Bambha et al., 2022). Conversely, children learning to read need to first unlearn mirror symmetries in order to differentiate characters from their mirrored version (Pegado et al., 2011; Perea et al., 2011). Abilities to capture specific problem symmetries may, however, be partially or fully innate in some animals. A study on chicks show that they have the ability to recognize an unknown synthetic 3D object from birth, across multiple points of view (Wood, 2013). This finding prompts us to reconsider whether humans and animals actively learn problem symmetries, or rely on neural architectures which are pre-configured for specific symmetries. It is at least clear from behavioral experiments that humans have the ability to adapt to unnatural symmetric transformations of their environment. Classically, Kohler and Erismann (Kohler, 1963) showed that a subject wearing goggles reversing the world upside down can adapt to this new environment after a few days of practice. The extent to which this adaptation is possible for new, previously unseen symmetries is unclear, however (e.g., what if the goggles permanently permuted the location of every pixel?). Finally, a direction of interest may be to imitate the physicist: by describing the world symbolically, the physicist comes to discover the symmetries of the world and exploit them for predictions. Language models and other neuro-symbolic approaches may be able to partly replicate this ability, or at least piggy-back on human accumulated knowledge about the symmetries of the world.

## Acknowledgments

We thank David Radnell, Milo Orlich, Samuel A. Ocko and Luigi Acerbi for useful discussions, Martin Trapp for comments on the manuscript, and Adityanarayanan Radhakrishnan for sharing with us his clear and concise lecture notes on neural kernels.

## References

- Abbas, A. and Deny, S. (2023). Progress and limitations of deep networks to recognize objects in unusual poses. *AAAI*.
- Ainsworth, S. K., Hayase, J., and Srinivasa, S. (2022). Git re-basin: Merging models modulo permutation symmetries. *arXiv preprint arXiv:2209.04836*.
- Alcorn, M. A., Li, Q., Gong, Z., Wang, C., Mai, L., Ku, W.-S., and Nguyen, A. (2019). Strike (with) a pose: Neural networks are easily fooled by strange poses of familiar objects. In *Proceedings of the IEEE/CVF Conference on Computer Vision and Pattern Recognition*.
- Anselmi, F., Evangelopoulos, G., Rosasco, L., and Poggio, T. (2019). Symmetry-adapted representation learning. *Pattern Recognition*.
- Anselmi, F., Manzoni, L., D’onofrio, A., Rodriguez, A., Caravagna, G., Bortolussi, L., and Cairoli, F. (2023). Data symmetries and learning in fully connected neural networks. *IEEE Access*, 11:47282–47290.
- Arora, S., Du, S. S., Hu, W., Li, Z., Salakhutdinov, R. R., and Wang, R. (2019). On exact computation with an infinitely wide neural net. *Advances in neural information processing systems*.
- Avidan, Y., Li, Q., and Sompolinsky, H. (2023). Connecting ntk and nngp: A unified theoretical framework for neural network learning dynamics in the kernel regime.
- Azulay, A. and Weiss, Y. (2019). Why do deep convolutional networks generalize so poorly to small image transformations? *Journal of Machine Learning Research*, 20(184):1–25.
- Bahri, Y., Dyer, E., Kaplan, J., Lee, J., and Sharma, U. (2024). Explaining neural scaling laws. *Proceedings of the National Academy of Sciences*.
- Bambha, V., Beckner, A., Shetty, N., Voss, A., Xie, J., Yiu, E., LoBue, V., Oakes, L., and Casasola, M. (2022). Developmental changes in children’s object insertions during play. *Journal of Cognition and Development*, 23(3):340–359.
- Bordelon, B., Canatar, A., and Pehlevan, C. (2020). Spectrum dependent learning curves in kernel regression and wide neural networks. In *Proceedings of the 37th International Conference on Machine Learning*.
- Bouchacourt, D., Ibrahim, M., and Deny, S. (2021). Addressing the topological defects of disentanglement via distributed operators.
- Brehmer, J., Behrends, S., de Haan, P., and Cohen, T. (2024). Does equivariance matter at scale?
- Bronstein, M. M., Bruna, J., Cohen, T., and Velicković, P. (2021). Geometric deep learning: Grids, groups, graphs, geodesics, and gauges.
- Canatar, A., Bordelon, B., and Pehlevan, C. (2021). Spectral bias and task-model alignment explain generalization in kernel regression and infinitely wide neural networks. *Nature communications*, 12(1):2914.
- Chauhan, V. K., Zhou, J., Lu, P., Molaei, S., and Clifton, D. A. (2024). A brief review of hypernetworks in deep learning. *Artificial Intelligence Review*.
- Chen, T., Kornblith, S., Norouzi, M., and Hinton, G. (2020). A simple framework for contrastive learning of visual representations. In *International conference on machine learning*, pages 1597–1607. PMLR.



- Chung, S., Lee, D. D., and Sompolinsky, H. (2018). Classification and geometry of general perceptual manifolds. *Physical Review X*, 8(3):031003.
- Cohen, T., Weiler, M., Kicanaoglu, B., and Welling, M. (2019). Gauge equivariant convolutional networks and the icosahedral CNN. In *Proceedings of the 36th International Conference on Machine Learning*.
- Cohen, T. and Welling, M. (2016). Group equivariant convolutional networks. In *Proceedings of The 33rd International Conference on Machine Learning*.
- Cohen, T. S., Geiger, M., Köhler, J., and Welling, M. (2018). Spherical CNNs. In *International Conference on Learning Representations*.
- Cohen, U., Chung, S., Lee, D. D., and Sompolinsky, H. (2020). Separability and geometry of object manifolds in deep neural networks. *Nature communications*, 11(1):746.
- Connor, M., Olshausen, B., and Rozell, C. (2024). Learning internal representations of 3d transformations from 2d projected inputs. *Neural Computation*, 36(11):2505–2539.
- Connor, M. and Rozell, C. (2020). Representing closed transformation paths in encoded network latent space. In *Proceedings of the AAAI Conference on Artificial Intelligence*, pages 3666–3675.
- Cranmer, M., Greydanus, S., Hoyer, S., Battaglia, P., Spergel, D., and Ho, S. (2020). Lagrangian neural networks. *arXiv preprint arXiv:2003.04630*.
- Culpepper, B. and Olshausen, B. (2009). Learning transport operators for image manifolds. *Advances in neural information processing systems*, 22.
- Dosovitskiy, A. (2020). An image is worth 16x16 words: Transformers for image recognition at scale. *arXiv preprint arXiv:2010.11929*.
- Dupont, E., Martin, M. B., Colburn, A., Sankar, A., Susskind, J., and Shan, Q. (2020). Equivariant neural rendering. In *International Conference on Machine Learning*, pages 2761–2770. PMLR.
- d’Ascoli, S., Touvron, H., Leavitt, M. L., Morcos, A. S., Biroli, G., and Sagun, L. (2021). Convit: Improving vision transformers with soft convolutional inductive biases. In *International conference on machine learning*, pages 2286–2296. PMLR.
- Elsayed, G., Ramachandran, P., Shlens, J., and Kornblith, S. (2020). Revisiting spatial invariance with low-rank local connectivity. In *International Conference on Machine Learning*, pages 2868–2879. PMLR.
- Farrell, M., Bordelon, B., Trivedi, S., and Pehlevan, C. (2021). Capacity of group-invariant linear readouts from equivariant representations: How many objects can be linearly classified under all possible views? *CoRR*.
- Finn, C., Abbeel, P., and Levine, S. (2017). Model-agnostic meta-learning for fast adaptation of deep networks. In *Proceedings of the 34th International Conference on Machine Learning*, Proceedings of Machine Learning Research.
- Finzi, M., Stanton, S., Izmailov, P., and Wilson, A. G. (2020). Generalizing convolutional neural networks for equivariance to lie groups on arbitrary continuous data. In *International Conference on Machine Learning*.
- Fort, S., Dziugaite, G. K., Paul, M., Kharaghani, S., Roy, D. M., and Ganguli, S. (2020). Deep learning versus kernel learning: an empirical study of loss landscape geometry and the time evolution of the neural tangent kernel. In *Advances in Neural Information Processing Systems*.
- Garrido, Q., Assran, M., Ballas, N., Bardes, A., Najman, L., and LeCun, Y. (2024). Learning and leveraging world models in visual representation learning.
- Geiping, J., Garrido, Q., Fernandez, P., Bar, A., Pirsiavash, H., LeCun, Y., and Goldblum, M. (2023). A cookbook of self-supervised learning. *arXiv preprint arXiv:2304.12210*.

- Gens, R. and Domingos, P. M. (2014). Deep symmetry networks. In *Advances in Neural Information Processing Systems*.
- Gerace, F., Saglietti, L., Mannelli, S. S., Saxe, A., and Zdeborová, L. (2022). Probing transfer learning with a model of synthetic correlated datasets. *Machine Learning: Science and Technology*, 3(1):015030.
- Gerken, J. E. and Kessel, P. (2024). Emergent equivariance in deep ensembles. In *Proceedings of the 41st International Conference on Machine Learning*.
- Goldt, S., Mézard, M., Krzakala, F., and Zdeborová, L. (2020). Modeling the influence of data structure on learning in neural networks: The hidden manifold model. *Physical Review X*, 10(4):041044.
- Gordon, J., Lopez-Paz, D., Baroni, M., and Bouchacourt, D. (2019). Permutation equivariant models for compositional generalization in language. In *International Conference on Learning Representations*.
- Greydanus, S., Dzamba, M., and Yosinski, J. (2019). Hamiltonian neural networks. *Advances in neural information processing systems*, 32.
- Gross, D. J. (1996). The role of symmetry in fundamental physics. *Proceedings of the National Academy of Sciences*, 93(25):14256–14259.
- Gruver, N., Finzi, M. A., Goldblum, M., and Wilson, A. G. (2023). The lie derivative for measuring learned equivariance. In *The Eleventh International Conference on Learning Representations*.
- Hajij, M., Zamzmi, G., Papamarkou, T., Miolane, N., Guzmán-Sáenz, A., Ramamurthy, K. N., Birdal, T., Dey, T. K., Mukherjee, S., Samaga, S. N., Livesay, N., Walters, R., Rosen, P., and Schaub, M. T. (2023). Topological deep learning: Going beyond graph data.
- Higgins, I., Amos, D., Pfau, D., Racaniere, S., Matthey, L., Rezende, D., and Lerchner, A. (2018). Towards a definition of disentangled representations.
- Humayun, A. I., Balestrieri, R., and Baraniuk, R. (2024). Deep networks always grok and here is why. In *High-dimensional Learning Dynamics 2024: The Emergence of Structure and Reasoning*.
- Ibrahim, M., Bouchacourt, D., and Morcos, A. (2022a). Robust self-supervised learning with lie groups.
- Ibrahim, M., Garrido, Q., Morcos, A., and Bouchacourt, D. (2022b). The robustness limits of sota vision models to natural variation. *arXiv preprint arXiv:2210.13604*.
- Jacot, A., Gabriel, F., and Hongler, C. (2018). Neural tangent kernel: Convergence and generalization in neural networks. In *Advances in Neural Information Processing Systems*.
- Jaderberg, M., Simonyan, K., Zisserman, A., et al. (2015). Spatial transformer networks. *Advances in neural information processing systems*.
- Kaba, S.-O. and Ravanbakhsh, S. (2023). Symmetry breaking and equivariant neural networks. In *NeurIPS 2023 Workshop on Symmetry and Geometry in Neural Representations*.
- Kaplan, J., McCandlish, S., Henighan, T., Brown, T. B., Chess, B., Child, R., Gray, S., Radford, A., Wu, J., and Amodei, D. (2020). Scaling laws for neural language models. *arXiv preprint arXiv:2001.08361*.
- Keller, T. A. and Welling, M. (2021a). Topographic vaes learn equivariant capsules. In *Advances in Neural Information Processing Systems*.
- Keller, T. A. and Welling, M. (2021b). Topographic vaes learn equivariant capsules. *Advances in Neural Information Processing Systems*, 34:28585–28597.
- Kohler, I. (1963). The formation and transformation of the perceptual world. *Psychological issues*.
- Lecun, Y., Bottou, L., Bengio, Y., and Haffner, P. (1998). Gradient-based learning applied to document recognition. *Proceedings of the IEEE*.

- Lee, J., Sohl-dickstein, J., Pennington, J., Novak, R., Schoenholz, S., and Bahri, Y. (2018). Deep neural networks as gaussian processes. In *International Conference on Learning Representations*.
- Liang, Q., Liu, Z., Ostrow, M., and Fiete, I. R. (2024). How diffusion models learn to factorize and compose. In *The Thirty-eighth Annual Conference on Neural Information Processing Systems*.
- Lippl, S. and Stachenfeld, K. (2024). When does compositional structure yield compositional generalization? a kernel theory.
- Madan, S., Henry, T., Dozier, J., Ho, H., Bhandari, N., Sasaki, T., Durand, F., Pfister, H., and Boix, X. (2022). When and how convolutional neural networks generalize to out-of-distribution category–viewpoint combinations. *Nature Machine Intelligence*.
- Madan, S., Sasaki, T., Li, T.-M., Boix, X., and Pfister, H. (2021). Small in-distribution changes in 3d perspective and lighting fool both cnns and transformers. *arXiv preprint arXiv:2106.16198*, 3.
- Mel, G. and Ganguli, S. (2021). A theory of high dimensional regression with arbitrary correlations between input features and target functions: sample complexity, multiple descent curves and a hierarchy of phase transitions. In *International Conference on Machine Learning*, pages 7578–7587. PMLR.
- Mercatali, G., Freitas, A., and Garg, V. (2022). Symmetry-induced disentanglement on graphs. *Advances in neural information processing systems*, 35:31497–31511.
- Moskalev, A., Sepiarskaia, A., Bekkers, E. J., and Smeulders, A. W. (2023). On genuine invariance learning without weight-tying. In *Proceedings of 2nd Annual Workshop on Topology, Algebra, and Geometry in Machine Learning (TAG-ML)*.
- Neal, R. M. (1996a). Bayesian learning for neural networks. *Lecture Notes in Statistics*, Springer.
- Neal, R. M. (1996b). Priors for infinite networks. *Bayesian learning for neural networks*, pages 29–53.
- Noether, E. (1918). Invariante variationsprobleme. *Nachrichten von der Gesellschaft der Wissenschaften zu Göttingen, Mathematisch-Physikalische Klasse*, 1918:235–257.
- Nordenfors, O. and Flinth, A. (2024). Ensembles provably learn equivariance through data augmentation.
- Novak, R., Xiao, L., Hron, J., Lee, J., Alemi, A. A., Sohl-Dickstein, J., and Schoenholz, S. S. (2020). Neural tangents: Fast and easy infinite neural networks in python. In *International Conference on Learning Representations*.
- Ollikka, N., Abbas, A., Perin, A., Kilpeläinen, M., and Deny, S. (2024). A comparison between humans and ai at recognizing objects in unusual poses. *arXiv preprint arXiv:2402.03973*.
- Ortiz-Jiménez, G., Modas, A., Moosavi, S.-M., and Frossard, P. (2020). Neural anisotropy directions. *Advances in Neural Information Processing Systems*, 33:17896–17906.
- Pegado, F., Nakamura, K., Cohen, L., and Dehaene, S. (2011). Breaking the symmetry: Mirror discrimination for single letters but not for pictures in the visual word form area. *NeuroImage*, 55(2):742–749.
- Perea, M., Moret-Tatay, C., and Panadero, V. (2011). Suppression of mirror generalization for reversible letters: Evidence from masked priming. *Journal of Memory and Language*, 65(3):237–246.
- Pfau, D., Higgins, I., Botev, A., and Racanière, S. (2020). Disentangling by subspace diffusion. In *Advances in Neural Information Processing Systems*.
- Power, A., Burda, Y., Edwards, H., Babuschkin, I., and Misra, V. (2022). Grokking: Generalization beyond overfitting on small algorithmic datasets. *arXiv preprint arXiv:2201.02177*.
- Sabour, S., Frosst, N., and Hinton, G. E. (2017). Dynamic routing between capsules. *Advances in neural information processing systems*.

- Sanborn, S., Shewmake, C. A., Olshausen, B., and Hillar, C. J. (2023). Bispectral neural networks. In *The Eleventh International Conference on Learning Representations*.
- Saxe, A. M., McClelland, J. L., and Ganguli, S. (2019). A mathematical theory of semantic development in deep neural networks. *Proceedings of the National Academy of Sciences*, 116(23):11537–11546.
- Schott, L., Von Kügelgen, J., Träuble, F., Gehler, P., Russell, C., Bethge, M., Schölkopf, B., Locatello, F., and Brendel, W. (2021). Visual representation learning does not generalize strongly within the same domain. *arXiv preprint arXiv:2107.08221*.
- Schuhmann, C., Beaumont, R., Vencu, R., Gordon, C., Wightman, R., Cherti, M., Coombes, T., Katta, A., Mullis, C., Wortsman, M., et al. (2022). Laion-5b: An open large-scale dataset for training next generation image-text models. *Advances in Neural Information Processing Systems*, 35:25278–25294.
- Shah, H., Tamuly, K., Raghunathan, A., Jain, P., and Netrapalli, P. (2020). The pitfalls of simplicity bias in neural networks. *Advances in Neural Information Processing Systems*, 33:9573–9585.
- Shepard, R. N. and Metzler, J. (1971). Mental rotation of three-dimensional objects. *Science*.
- Siddiqui, S. A., Krueger, D., and Breuel, T. (2023). Investigating the nature of 3d generalization in deep neural networks.
- Simsek, B., Ged, F., Jacot, A., Spadaro, F., Hongler, C., Gerstner, W., and Brea, J. (2021). Geometry of the loss landscape in overparameterized neural networks: Symmetries and invariances. In *Proceedings of the 38th International Conference on Machine Learning*.
- Singh, M., Gustafson, L., Adcock, A., Reis, V. d. F., Gedik, B., Kosaraju, R. P., Mahajan, D., Girshick, R., Dollár, P., and van der Maaten, L. (2022). Revisiting Weakly Supervised Pre-Training of Visual Perception Models. In *CVPR*.
- Sohl-Dickstein, J., Wang, C. M., and Olshausen, B. A. (2010). An unsupervised algorithm for learning lie group transformations. *arXiv preprint arXiv:1001.1027*.
- Sorscher, B., Ganguli, S., and Sompolinsky, H. (2022). Neural representational geometry underlies few-shot concept learning. *Proceedings of the National Academy of Sciences*, 119(43):e2200800119.
- Stanley, K. O. and Miikkulainen, R. (2002). Evolving neural networks through augmenting topologies. *Evolutionary Computation*.
- Sun, C., Shrivastava, A., Singh, S., and Gupta, A. (2017). Revisiting unreasonable effectiveness of data in deep learning era. In *Proceedings of the IEEE International Conference on Computer Vision (ICCV)*.
- Sundaram, S., Sinha, D., Groth, M., Sasaki, T., and Boix, X. (2021). Symmetry perception by deep networks: inadequacy of feed-forward architectures and improvements with recurrent connections. *arXiv preprint arXiv:2112.04162*.
- Tanaka, H. and Kunin, D. (2021). Noether’s learning dynamics: Role of symmetry breaking in neural networks. In *Advances in Neural Information Processing Systems*.
- Valle-Perez, G., Camargo, C. Q., and Louis, A. A. (2019). Deep learning generalizes because the parameter-function map is biased towards simple functions. In *International Conference on Learning Representations*.
- Wang, R., Walters, R., and Yu, R. (2022). Approximately equivariant networks for imperfectly symmetric dynamics. In *International Conference on Machine Learning*, pages 23078–23091. PMLR.
- Wiedemer, T., Mayilvahanan, P., Bethge, M., and Brendel, W. (2024). Compositional generalization from first principles. *Advances in Neural Information Processing Systems*, 36.
- Wood, J. N. (2013). Newborn chickens generate invariant object representations at the onset of visual object experience. *Proceedings of the National Academy of Sciences*, 110(34):14000–14005.

- Worrall, D. E., Garbin, S. J., Turmukhambetov, D., and Brostow, G. J. (2017). Harmonic networks: Deep translation and rotation equivariance. In *2017 IEEE Conference on Computer Vision and Pattern Recognition (CVPR)*.
- Yang, G. and Hu, E. J. (2020). Feature learning in infinite-width neural networks. *arXiv preprint arXiv:2011.14522*.
- Yang, G., Yu, D., Zhu, C., and Hayou, S. (2023). Tensor programs vi: Feature learning in infinite-depth neural networks.
- Yeh, R. A., Hu, Y.-T., Hasegawa-Johnson, M., and Schwing, A. (2022). Equivariance discovery by learned parameter-sharing. In *Proceedings of The 25th International Conference on Artificial Intelligence and Statistics*.
- Zbontar, J., Jing, L., Misra, I., LeCun, Y., and Deny, S. (2021). Barlow twins: Self-supervised learning via redundancy reduction. In *International conference on machine learning*, pages 12310–12320. PMLR.
- Zemel, R. and Hinton, G. E. (1990). Discovering viewpoint-invariant relationships that characterize objects. In *Advances in Neural Information Processing Systems*.
- Zhang, C., Bengio, S., Hardt, M., Recht, B., and Vinyals, O. (2021). Understanding deep learning (still) requires rethinking generalization. *Communications of the ACM*, 64(3):107–115.
- Zhou, A., Knowles, T., and Finn, C. (2021). Meta-learning symmetries by reparameterization. In *International Conference on Learning Representations*.
- Ziyin, L., Hartwig, T., and Ueda, M. (2020). Neural networks fail to learn periodic functions and how to fix it. *Advances in Neural Information Processing Systems*, 33:1583–1594.



# Appendix

## Appendix Contents

<b>A Derivation of the spectral error</b>	<b>25</b>
A.1 Extension to multiple missing points . . . . .	29
<b>B Architecture details</b>	<b>30</b>
B.1 Architectures used in Fig. 1 . . . . .	30
B.2 Architectures trained on pairs of orbits from MNIST . . . . .	30
B.3 Architecture trained on multiple seeds and multiple classes of rotated-MNIST . . . . .	31
<b>C Extension of the spectral theory to equivariant architectures</b>	<b>32</b>
<b>D Varying the number of angles in an orbit</b>	<b>36</b>
<b>E Further MLP analyses</b>	<b>37</b>
<b>F Multiple seeds, multiple classes - additional figures</b>	<b>39</b>
<b>G Further Convolutional NTK (CNTK) analyses</b>	<b>40</b>
G.1 Rotation orbits . . . . .	40
G.2 Translation orbits . . . . .	41

All code is available at <https://github.com/Andrea-Perin/gpsymm>.

## A Derivation of the spectral error

In this section, we report the computations that give the spectral error in Eq. 7. We start by describing general Gaussian process (GP) regression, and then move to the actual derivation of our formula, that applies specifically to a group-cyclic dataset.

We consider a dataset  $\mathcal{D} = \{(x_i, y_i)\}_{i=1}^N \subset \mathbb{R}^d \times \mathbb{R}$ , so that the samples  $x_i$  are  $d$  dimensional vectors and labels  $y_i$  are scalars.

GP regression is a Bayesian method which, starting from the user's prior information (namely, a mean function  $m : \mathcal{X} \rightarrow \mathbb{R}$ , and a covariance function  $k : \mathcal{X} \times \mathcal{X} \rightarrow \mathbb{R}$ ), produces a distribution of regression functions of the type  $f : \mathcal{X} \rightarrow \mathbb{R}$ . We are interested in the value of such a function at a given test point  $x_t \in \mathcal{X}$ , conditioned on the values  $(x_i, y_i)$  contained in the dataset. To obtain these pointwise results, one can focus on a finite collection of points  $(x_i, y_i) \in \mathcal{X} \times \mathbb{R}$ . Any such finite collection has the property (inherited by the GP) of being jointly Gaussian-distributed as follows:

$$(y_1, \dots, y_N) \sim \mathcal{N}(\vec{m}, K), \quad (19)$$

where  $\vec{m}_i = m(x_i) \in \mathbb{R}$  is the mean vector, obtained by evaluating the mean function  $m$  over the given points, and  $K_{ij} = k(x_i, x_j) \in \mathbb{R}$  is the covariance matrix, obtained by evaluating the covariance function  $k$  over all pairs of points  $x_i, x_j$  that can be formed in the collection. We set  $m(x) = 0$  everywhere.

Equipped with these tools, we can formulate regression on an additional test point  $x_t$  as a *conditioning* over a  $N + 1$  dimensional multivariate Gaussian distribution (MVG), in order to obtain a probability distribution for the value of  $y_t$ . In other words, we can consider the set of  $N + 1$  samples ( $N$  from the training set, and the additional one being the test value) to be distributed according to a  $N + 1$  dimensional MVG:

$$(y_1, \dots, y_N, y_t) \sim \mathcal{N}\left(0, \begin{bmatrix} K & k(\vec{x}, x_t) \\ k(\vec{x}, x_t)^T & k(x_t, x_t) \end{bmatrix}\right), \quad (20)$$

where we use the notation  $k(\vec{x}, x_t) \in \mathbb{R}^N$  to denote the column vector that, at  $i$ -th entry, contains  $k(x_i, x_t)$  with  $x_i$  being the  $i$ -th sample in the dataset. The conditional mean and variance for  $y_t$  are described by the formulas:

$$\mu_{t|\mathcal{D}} = (K^{-1}k(\vec{x}, x_t))^T \vec{y}, \quad (21)$$

$$\sigma_{t|\mathcal{D}} = k(x_t, x_t) - (K^{-1}k(\vec{x}, x_t))^T k(\vec{x}, x_t), \quad (22)$$

where we define  $\vec{y}$  to be the vector of the training labels. The expectation of this distribution (i.e.,  $\mu_{t|\mathcal{D}}$ ) will then serve as the result of the Gaussian process regression. This procedure can be extended for  $p$  test points, with all the opportune dimensionality changes (i.e., the result of the conditioning will be a  $p$  dimensional MVG).

In Section 3.2, we take the Gaussian (RBF) kernel as the kernel for Gaussian Process regression. In later sections, we consider various deep network architectures in the infinite width limit. These also behave like Gaussian Processes, with a kernel that is specified by their architecture (Jacot et al., 2018; Neal, 1996b). Our proof for the spectral formula of the generalization error does not depend on the specific kernel used, as long as the kernel matrix is *circulant over a group of points generated by the action of a cyclic group*. We demonstrate elsewhere that this is the case both for the Gaussian kernel, as well as all the deep neural kernels that we analyze in this paper (MLP and ConvNets).

We are now ready to present the derivation of Eq. 7. We start by presenting a depiction of the conditioning procedure for the case in which the training set consists of a single point (Fig. 8a). In the following, we denote labels as  $y_0$  and  $y_1$ , and their respective values as  $\mu_0$  and  $\mu_1$ . In practice, the  $y$ s are the training set labels, and the  $\mu$ s are their values. In this case, the training label is  $y_0$ , while the test label is  $y_1$ . The two labels are jointly distributed according to a 2 dimensional Gaussian, with mean 0 and covariance matrix  $K$ . This matrix depends on the values of  $x_0, x_1$ , and the kernel function  $k$ . We represent the distribution as an ellipse, which is understood as a level set of the covariance matrix  $K$ , centered at the mean, 0, in a way similar to the usual representation of confidence levels of a multivariate Gaussian distribution. Conditioning over the known training label  $y_0$  can be interpreted geometrically as slicing the ellipse with a vertical line at coordinate  $\mu_0$ . We thus obtain a segment (i.e., a 1-dimensional ellipse), the midpoint of which is the point  $(\mu_0, \mu_{1|0})$ , where  $\mu_{1|0}$  denotes the conditional value of  $y_1$  given  $x_0, x_1$  and the value of  $y_0$ . As a consequence, the result of GP regression can thus be interpreted geometrically as finding the  $y_1$  coordinate of the center of the slice. Doing this will reward us with Eq. 7.

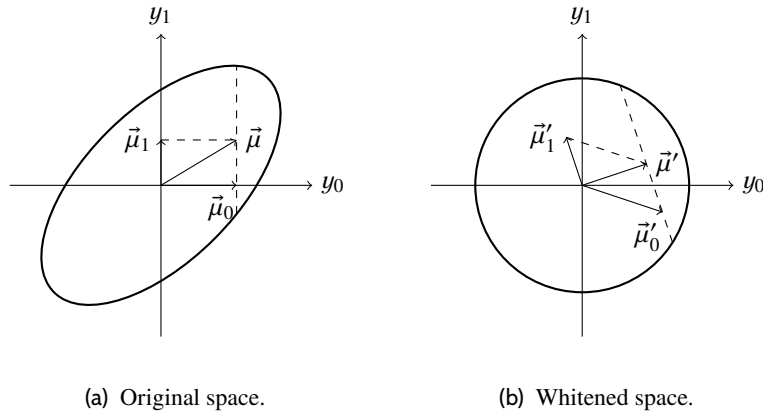


Figure 8. 2D sketch of the geometric interpretation, showing the effect of the whitening transformation.

We can make this geometric task easier by turning the ellipse into a circle; we can do this by performing a *whitening* operation on this vector space. Such whitening is effectively obtained by the inverse of the square root of the covariance matrix  $K$ . Denoting the transformed values by priming them, our task is now to find  $\vec{\mu}'_1$  given  $\vec{\mu}'_0$ <sup>6</sup>. It is clear that the segment produced by the conditioning turns now into a chord of the circle. This makes the whitened vector  $\vec{\mu}'$ , which is defined so that it points to the midpoint of the

<sup>6</sup>We have now shifted to a vector notation for these values as, unlike in the original space, both components can be nonzero.

segment, *perpendicular* to the segment itself. This means we can write the following geometric condition:

$$(\vec{\mu}'_0 + \vec{\mu}'_1) \cdot \vec{\mu}'_1 = 0. \quad (23)$$

The same properties hold in the case where we have  $2N$  samples, as in the main text, and we condition on  $2N - 1$  of them. Let us now denote the value we wish to infer as  $\mu_0$ ; the multidimensional extension of Eq. 23 becomes

$$\left( \sum_{i=0}^{2N-1} \vec{\mu}'_i \right) \cdot \vec{\mu}'_0 = 0. \quad (24)$$

We now move to solve Eq. 24. To do so, we make the justified assumption that  $K$  is *circulant* (as a consequence of the group-symmetric structure of the dataset). As such, it is diagonalized by the Discrete Fourier Transform (DFT) basis,  $E$ :

$$K = E^{-1} \Lambda E. \quad (25)$$

Whitening is obtained by applying the transform given by:

$$Z = K^{-1/2} = E \Lambda^{-1/2} E^{-1}, \quad (26)$$

to all the vectors  $\vec{\mu}_i$ .

To make computations easier, we collect our vectors in a data matrix  $M$  so that the  $i$ -th column is  $\vec{\mu}_i$ , we can collectively transform our samples with a matrix operation. The collection of transformed (i.e., whitened) samples is denoted as  $M'$ , and

$$M' = ZM. \quad (27)$$

We now write down a few properties of the matrices at play that will make computations quicker. Denoting  $\delta$  as the Kronecker delta,  $\lambda_i$  as the  $i$ -th eigenvalue of  $K$ , and  $\omega = \exp(-2\pi i/(2N))$ , we have

$$M_{ij} = \mu_i \delta_{ij}, \quad (28)$$

$$E_{ij} = \frac{1}{\sqrt{2N}} \omega^{ij}, \quad (29)$$

$$E_{ij}^{-1} = \frac{1}{\sqrt{2N}} \omega^{-ij}, \quad (30)$$

$$\Lambda_{ij}^{-1/2} = \frac{1}{\sqrt{\lambda_i}} \delta_{ij}. \quad (31)$$

We can now compute the value of the  $j$ -th component of the  $i$ -th sample in whitened space, that is,  $M'_{ji}$ :

$$M'_{ji} = (ZM)_{ji} \quad (32)$$

$$= \sum_k Z_{jk} M_{ki} \quad (33)$$

$$= \sum_k (E \Lambda^{-1} E^{-1})_{jk} M_{ki} \quad (34)$$

$$= \sum_{klm} E_{jl} \Lambda_{lm}^{-1/2} E_{mk}^{-1} M_{ki} \quad (35)$$

$$= \sum_{klm} \frac{1}{\sqrt{2N}} \omega^{jl} \frac{1}{\sqrt{\lambda_l}} \delta_{lm} \frac{1}{\sqrt{2N}} \omega^{-mk} \mu_k \delta_{ki} \quad (36)$$

$$= \sum_l \frac{1}{2N} \omega^{jl} \frac{1}{\sqrt{\lambda_l}} \omega^{-li} \mu_i \quad (37)$$

$$= \sum_l \frac{1}{2N} \frac{\mu_i \omega^{l(j-i)}}{\sqrt{\lambda_l}}. \quad (38)$$

We can now take Eq. 24 and distribute the dot product over the sum. We obtain:

$$\sum_{i=0}^{2N-1} \sum_j M'_{ji} M'_{j0} = 0. \quad (39)$$

In general,

$$\sum_j M'_{ji} M'_{j0} = \sum_j \left( \sum_l \frac{1}{2N} \frac{\mu_i \omega^{l(j-i)}}{\sqrt{\lambda_l}} \right) \left( \sum_k \frac{1}{2N} \frac{\mu_0 \omega^{kj}}{\sqrt{\lambda_k}} \right) \quad (40)$$

$$= \sum_{lkj} \frac{1}{(2N)^2} \mu_i \mu_0 \frac{\omega^{l(j-i)} \omega^{kj}}{\sqrt{\lambda_l \lambda_k}} \quad (41)$$

$$= \sum_{lkj} \frac{1}{2N} \frac{\mu_i \mu_0 \omega^{-il}}{\sqrt{\lambda_l \lambda_k}} \frac{1}{2N} \omega^{j(l+k)}. \quad (42)$$

We isolate the rightmost term and use the equality

$$\sum_j \frac{1}{2N} \omega^{j(l+k)} = \delta_{l, 2N-k}. \quad (43)$$

Thus, we get

$$\sum_j M'_{ji} M'_{j0} = \sum_{kl} \frac{1}{2N} \frac{\mu_i \mu_0 \omega^{-il}}{\sqrt{\lambda_l \lambda_k}} \delta_{l, 2N-k} \quad (44)$$

$$= \sum_k \frac{1}{2N} \frac{\mu_i \mu_0 \omega^{-i(2N-k)}}{\sqrt{\lambda_{2N-k} \lambda_k}} \quad (45)$$

$$= \sum_k \frac{1}{2N} \frac{\mu_i \mu_0 \omega^{ik}}{\lambda_k}. \quad (46)$$

Thus, Eq. 39 becomes, after simplifying the common term  $\mu_0$  away,

$$\sum_{i=0}^{2N-1} \sum_k \frac{1}{2N} \frac{\mu_i \omega^{ik}}{\lambda_k} = 0. \quad (47)$$

So far, we have only used the circularity of  $K$  in our derivation. We now make an additional assumption, this time on the values and ordering of the labels. We require  $\mu_{2i} = \mu$ , and  $\mu_{2i+1} = -\mu$  for  $i \in [0, \dots, N-1]$ . This amounts to having our samples be interleaved and have opposing labels. We can then write the general expression for the value of  $\mu_i$ , valid for all  $i$ :

$$\mu_i = \mu \omega^{iN} + (\mu_0 - \mu) \delta_{i0}. \quad (48)$$

Note how, for  $i = 0$  (that is, the missing point) we recover the unknown value  $\mu_0$  for which we want to solve. With this substitution, we get

$$\sum_{i=0}^{2N-1} \frac{1}{2N} (\mu \omega^{iN} + (\mu_0 - \mu) \delta_{i0}) \sum_k \frac{\omega^{ik}}{\lambda_k} = 0. \quad (49)$$

The summation thus splits in three parts:

$$\sum_{i=0}^{2N-1} \frac{\mu}{N} \sum_k \frac{\omega^{i(k+N)}}{\lambda_k} + \sum_{i=0}^{2N-1} \frac{\mu_0}{2N} \sum_k \frac{\omega^{ik}}{\lambda_k} \delta_{i0} - \sum_{i=0}^{2N-1} \frac{\mu}{2N} \delta_{i0} \sum_k \frac{\omega^{ik}}{\lambda_k} = 0 \quad (50)$$

We now go over each of them.

- For the first term,

$$\sum_{i=0}^{2N-1} \sum_k \frac{\mu}{2N} \frac{\omega^{i(k+N)}}{\lambda_k} = \mu \sum_k \frac{1}{\lambda_k} \sum_{i=0}^{2N-1} \frac{1}{2N} \omega^{i(k+N)} \quad (51)$$

$$= \mu \sum_k \frac{1}{\lambda_k} \delta_{k,-N} \quad (52)$$

$$= \mu \frac{1}{\lambda_N}. \quad (53)$$

- The second term contains a Kronecker delta that selects the 0-th component in the sum over index  $i$ . Thus, we get

$$\mu_0 \sum_k \frac{1}{2N} \frac{1}{\lambda_k} = \mu_0 \langle \lambda^{-1} \rangle, \quad (54)$$

where the angled brackets denote the average.

- The last term, like the previous one, contains a selection on  $i$  due to the Kronecker delta. It becomes

$$\mu \langle \lambda^{-1} \rangle. \quad (55)$$

Putting all together, we get

$$\mu \frac{1}{\lambda_N} + \mu_0 \langle \lambda^{-1} \rangle - \mu \langle \lambda^{-1} \rangle = 0, \quad (56)$$

from which, after rearranging, we get a formula for our missing point as a function of the eigenvalues of  $K$ :

$$\mu_0 = \mu \left( 1 - \frac{\lambda_N^{-1}}{\langle \lambda^{-1} \rangle} \right). \quad (57)$$

The formula for the spectral error, then, assuming  $\mu = 1$ , is

$$\varepsilon_s = \frac{\lambda_N^{-1}}{\langle \lambda^{-1} \rangle}. \quad (58)$$

## A.1 Extension to multiple missing points

In the case of multiple missing points, we can find an equivalent of Eq. 58. It requires solving an  $p$  dimensional linear system, where  $p$  is the number of missing points.

We denote by  $[p]$  the set of indexes for the missing points. Then, for the missing point with index  $j \in [p]$ , we have

$$\sum_{m \in [p]} \mu_m \frac{1}{2N} \sum_l \frac{\omega^{l(j-m)}}{\lambda_l} = \mu \left( \frac{1}{2N} \sum_{n \in [p]} \omega^{nN} \sum_k \frac{\omega^{k(j-n)}}{\lambda_k} - \frac{\omega^{jN}}{\lambda_N} \right). \quad (59)$$

We notice that this equation can be expressed as the following linear system:

$$\sum_{m \in [p]} A_{jm} \mu_m = b_j, \quad (60)$$

where

$$A_{jm} = \frac{1}{2N} \sum_l \frac{\omega^{l(j-m)}}{\lambda_l}, \quad b_j = \mu \left( \frac{1}{2N} \sum_{n \in [p]} \omega^{nN} \sum_k \frac{\omega^{k(j-n)}}{\lambda_k} - \frac{\omega^{jN}}{\lambda_N} \right). \quad (61)$$

One can check that, if we set  $[p] = \{0\}$ , this formula recovers the expression in Eq. 58.

## B Architecture details

All the relevant code can be found at <https://github.com/Andrea-Perin/gpsymm>.

### B.1 Architectures used in Fig. 1

For Fig. 1, we used the following architectures. We used the default initialization scheme provided by PyTorch (a version of Kaiming uniform).

- a MLP (the Rearrange layer is provided by the [einops](#) library):

```

1     m = nn.Sequential(
2         Rearrange('b 1 h w -> b (h w)'),
3         nn.Linear(1*28*28, 512, bias=True),
4         nn.ReLU(),
5         nn.Dropout(),
6         nn.Linear(512, 128, bias=True),
7         nn.ReLU(),
8         nn.Dropout(),
9         nn.Linear(128, 10, bias=False),
10        nn.LogSoftmax(dim=1)
11    )

```

- a ConvNet:

```

1     c = nn.Sequential(
2         nn.Conv2d(1, 24, 5, 1),
3         nn.MaxPool2d(kernel_size=2),
4         nn.ReLU(),
5         nn.Conv2d(24, 32, kernel_size=3),
6         nn.MaxPool2d(kernel_size=2),
7         nn.ReLU(),
8         Rearrange('b c h w -> b (c h w)'),
9         nn.Linear(800, 256),
10        nn.ReLU(),
11        nn.Linear(256, 10),
12        nn.LogSoftmax(dim=1)
13    )

```

- a ViT-Simple (using the implementation provided by the library [vit-pytorch](#)):

```

1     v = SimpleViT(
2         image_size = 28,
3         patch_size = 4,
4         num_classes = 10,
5         dim = 256,
6         depth = 2,
7         heads = 4,
8         mlp_dim = 256,
9         channels=1
10    )

```

The models were trained for 20 epochs using the Adam optimizer, using a learning rate of  $1e-3$  and  $(\beta_1, \beta_2) = (0.7, 0.9)$ . Further details on the implementation can be found in the provided code.

### B.2 Architectures trained on pairs of orbits from MNIST

For all tests involving two orbits from MNIST, we used the following MLP architecture, where the parameters `args.n_hidden` defines the depth of the MLP (either 1 or 5).

```

1 W_std, b_std = 1., 1.
2 layer = nt.stax.serial(
3     nt.stax.Dense(512, W_std=W_std, b_std=b_std),
4     nt.stax.Relu(),
5 )
6 init_fn, apply_fn, kernel_fn = nt.stax.serial(
7     nt.stax.serial(*([layer] * args.n_hidden)),
8     nt.stax.Dense(1, W_std=W_std, b_std=b_std)
9 )

```

For all tests involving two orbits from MNIST, we used the following Convolutional architecture, where the parameter `args.kernel_size` defines the size of the conv kernel, and `IS_GAP` defines whether or not to include the `GlobalAvgPool` layer.

```

1 W_std, b_std = 1., 1.
2 conv = nt.stax.serial(
3     nt.stax.Conv(
4         out_chan=64,
5         filter_shape=(args.kernel_size, args.kernel_size),
6         padding='CIRCULAR',
7         W_std=W_std, b_std=None),
8     nt.stax.Relu()
9 )
10 pool = nt.stax.GlobalAvgPool() if IS_GAP else nt.stax.Identity()
11 init_fn, apply_fn, kernel_fn = nt.stax.serial(
12     conv,
13     pool,
14     nt.stax.Flatten(),
15     nt.stax.Dense(1, W_std=W_std, b_std=None)
16 )

```

### B.3 Architecture trained on multiple seeds and multiple classes of rotated-MNIST

For Section 3.4, we use the following network architecture and optimizer. Note how this architecture is not in principle trainable with a cross-entropy loss, as it outputs a scalar value. This is needed for the computation of our kernel function. The actual training, which indeed is based on the cross-entropy loss, involves *all but the last two layers*, i.e., the last `Relu` and `Dense` layers. This is done by basic model surgery techniques, made possible by the simple sequential structure of the model.

```

1 def net_maker(
2     W_std: float = 1.,
3     b_std: float = 1.,
4     dropout_rate: float = 0.5,
5     mode: str = 'train'
6 ):
7     return nt.stax.serial(
8         nt.stax.Dense(512, W_std=W_std, b_std=b_std),
9         nt.stax.Relu(),
10        nt.stax.Dropout(rate=dropout_rate, mode=mode),
11        nt.stax.Dense(128, W_std=W_std, b_std=b_std),
12        nt.stax.Relu(),
13        nt.stax.Dropout(rate=dropout_rate, mode=mode),
14        nt.stax.Dense(10, W_std=W_std, b_std=None),
15        nt.stax.Relu(),
16        nt.stax.Dense(1, W_std=W_std, b_std=b_std)
17    )
18
19 optim = optax.adam(learning_rate=1e-3, b1=0.7, b2=0.9)

```

## C Extension of the spectral theory to equivariant architectures

We study how the symmetries of the dataset interact with equivariant architectures. We limit our analysis to the Neural Network Gaussian Process (NNGP), as the Neural Tangent Kernel (NTK) adds extra terms that would cloud the derivations. Essentially, the same proofs should hold for the NTK.

We distinguish two cases: (1) when the neural network is equivariant to the symmetry of interest; (2) when the neural network is equivariant, but not to the symmetry of interest. The number of possible symmetries to consider is vast, as well as the number of possible equivariant architectures. Here, we study the interplay between equivariance and symmetries in a limited setup: we consider spatially convolutional neural networks, and we study their interplay with a dataset with translation symmetry (the symmetry to which the network is equivariant) and with a dataset with rotational symmetry. These examples should give the reader an intuition as to how these two things interact in general.

**Dataset with translational symmetry.** We consider a dataset composed of seed images and all their translations. For the purpose of the proofs to follow, we will focus on a single orbit of this dataset, which consists of a single seed point  $x_s \in \mathbb{R}^{n \times n}$  and all of its translations:

$$\mathcal{O}_T = \{g_T^0.x_s, g_T^1.x_s, \dots, g_T^{n-1}.x_s\}, \quad (62)$$

where the translation operator  $g_T$  acts on images by circularly shifting them along one of the dimensions. For pixel coordinates  $(i_x, i_y)$ , and the corresponding value of the pixel  $x(i_x, i_y)$ , we write:

$$g_T.x \left( \begin{bmatrix} i_x \\ i_y \end{bmatrix} \right) = x \left( \begin{bmatrix} (i_x + 1) \bmod n \\ i_y \end{bmatrix} \right). \quad (63)$$

**Dataset with rotational symmetry.** We consider a dataset composed of seed images and all their rotations in  $C_4$  (we limit ourselves to 4 cardinal rotations to avoid definitional problems of image rotation on discrete pixel grids). We will focus on a single orbit of this dataset, which consists in a single seed point  $x_s \in \mathbb{R}^{n \times n}$  and all its rotations:

$$\mathcal{O}_R = \{g_R^0.x_s, g_R^1.x_s, g_R^2.x_s, g_R^3.x_s\} \quad (64)$$

where the rotation operator  $g_R$  permutes pixel coordinates  $(i_x, i_y)$  as follows:

$$g_R.x \left( \begin{bmatrix} i_x \\ i_y \end{bmatrix} \right) = x \left( \begin{bmatrix} i_y \\ n - i_x \end{bmatrix} \right). \quad (65)$$

We also distinguish between two types of convolutional architectures: (1) convolutional architectures where the last layer is fully connected: these architectures do not ensure full invariance to translation; (2) convolutional architectures where the last layer does global average pooling, ensuring invariance to translation.

**Fully connected convolutional network (FC).** We consider a fully connected convolutional network with one hidden layer, filters of size  $3 \times 3$ , circular padding and stride of 1. The network  $f : \mathbb{R}^{n \times n} \rightarrow \mathbb{R}$  is parameterized by:

$$f_{\text{FC}}(x) = A \frac{1}{\sqrt{k}} \phi(B \otimes x)_v, \quad (66)$$

where  $A \in \mathbb{R}^{1 \times n^2 k}$ ,  $B \in \mathbb{R}^{k \times 1 \times 3 \times 3}$ ,  $\otimes$  denotes the spatial convolution operation, and for any matrix  $u \in \mathbb{R}^{n \times n}$ ,  $u_v \in \mathbb{R}^{n^2}$  denotes the vectorization (i.e., flattening) of  $u$ . This network first applies a convolutional layer to the data, then flattens the resulting representation into a vector, and passes it through a fully connected layer.

Let  $K \in \mathbb{R}^{n^2 \times n^2}$  denote the Conv-NNGP for a 1-layer fully convolutional network operating on a pair of images  $x, x'$  of size  $n \times n$ . This kernel contains an entry for every coordinate quadruplet  $(i_x, i_y, i'_x, i'_y)$  across the images  $x, x'$ . On the other hand, the Conv-NNGP of the network above  $f_{\text{FC}}$  reduces this representation to a kernel of size  $K_{\text{FC}} \in \mathbb{R}$ , by letting  $K_{\text{FC}} = \text{Tr}(K)$  (Arora et al., 2019):



$$K_{FC}(x, x') = \sum_{i_x, i_y} K_{i_x, i_y, i_x, i_y}(x, x') \quad (67)$$

$$= \sum_{i_x, i_y} \sum_k \left\langle \phi(B_{k, i_x, i_y} \cdot x), \phi(B_{k, i_x, i_y} \cdot x') \right\rangle_{\Theta} \quad (68)$$

where  $k$  denotes the filter index, and  $\langle \cdot, \cdot \rangle_{\Theta}$  the average dot product of the embeddings over the randomly sampled weights of the models.

**Global Average Pooling convolutional network (GAP).** We consider a convolutional network with global average pooling at the last layer. This network is invariant to discrete translations. We consider the network  $f_{GAP} : \mathbb{R}^{n \times n} \rightarrow \mathbb{R}$  be parameterized by:

$$f_{GAP}(x) = \frac{1}{\sqrt{k}n^2} \sum_k \sum_{i_x} \sum_{i_y} A_{1k} \phi(B_{k, i_x, i_y} \cdot x) \quad (69)$$

where  $A \in \mathbb{R}^{1 \times k}$ , and  $B \in \mathbb{R}^{k \times 1 \times 3 \times 3}$  with  $B_k \in \mathbb{R}^{1 \times 1 \times 3 \times 3}$  indexing filter  $k$  of  $B$ .  $B_{k, i_x, i_y} \in \mathbb{R}^{1 \times 1 \times n \times n}$  is obtained by centering  $B_k$  at coordinates  $(i_x, i_y)$  of an  $n \times n$  grid with periodic boundary conditions, and filling the remaining entries with zeros. Then, the dot product is understood as the sum of the elementwise multiplications of all entries of  $x$  and  $B_{k, i_x, i_y}$ . We remark that this operation is effectively an alternative way of describing a convolution with filter bank  $B$ , but this indexing choice proves useful in the proofs. After applying a convolutional layer to the data, this network averages the resulting representation across each of the  $k$  output channels, and then takes a linear combination of these averages using a fully connected layer.

The Conv-NNGP of  $f_{GAP}$  reduces  $K$  to  $K_{GAP}$  by letting  $K_{GAP} = \frac{1}{n^4} \sum_{i_x, i_y, i'_x, i'_y} K_{i_x, i_y, i'_x, i'_y}$  (i.e., averaging over all elements of  $K$ ). In the following, we omit this prefactor  $1/n^4$  for notational convenience.

$$K_{GAP}(x, x') = \sum_{\substack{i_x, i_y \\ i'_x, i'_y}} K_{i_x, i_y, i'_x, i'_y}(x, x') \quad (70)$$

$$= \sum_{\substack{i_x, i_y \\ i'_x, i'_y}} \sum_k \left\langle \phi(B_{k, i_x, i_y} \cdot x), \phi(B_{k, i'_x, i'_y} \cdot x') \right\rangle_{\Theta} \quad (71)$$

**Proposition 1.** *The kernel matrix of a fully connected convolutional network  $K_{FC}$  over a translation orbit  $O_T$  is circulant. Moreover, this kernel matrix is in general not constant or rank-deficient.*

*Proof.* We first show that the kernel of a fully connected network is circulant over an orbit of image rotations. Consider a pair of images from this orbit  $(x, x') \in O_T$ . We show below that applying the same image rotation  $g_T$  to both these images leaves the kernel unaffected, which is equivalent to showing that the kernel matrix is circulant over the orbit  $O_T$ . First, we write:

$$K_{FC}(g_T \cdot x, g_T \cdot x') = \sum_{i_x, i_y} \sum_k \left\langle \phi(B_{k, i_x, i_y} \cdot g_T \cdot x), \phi(B_{k, i_x, i_y} \cdot g_T \cdot x') \right\rangle_{\Theta} \quad (72)$$

$$= \sum_{i_x, i_y} \sum_k \left\langle \phi(g_T^{-1} \cdot B_{k, i_x, i_y} \cdot x), \phi(g_T^{-1} \cdot B_{k, i_x, i_y} \cdot x') \right\rangle_{\Theta} \quad (73)$$

Applying a translation to image  $x$  is equivalent to applying a change of spatial index to the convolutional filters,  $g_T^{-1} \cdot B_{k, i_x, i_y} = B_{k, i_x - 1 \bmod n, i_y}$ , such that:

$$K_{FC}(g_T \cdot x, g_T \cdot x') = \sum_{i_x, i_y} \sum_k \left\langle \phi(B_{k, i_x - 1 \bmod n} \cdot x), \phi(B_{k, i_x - 1 \bmod n, i_y} \cdot x') \right\rangle_{\Theta} \quad (74)$$

We operate the changes of variable with renaming  $i_x \leftarrow i_x - 1 \pmod n$ :

$$K_{\text{FC}}(g_T \cdot x, g_T \cdot x') = \sum_{i_x, i_y} \sum_k \left\langle \phi(B_{k, i_x, i_y} \cdot x), \phi(B_{k, i_x, i_y} \cdot x') \right\rangle_{\Theta} \quad (75)$$

$$= K_{\text{FC}}(x, x') \quad (76)$$

This concludes our proof that the kernel of a fully connected convolutional network is circulant over an orbit of image translations.

Another question of interest is whether the kernel is constant over pairs of images belonging to the same orbit. Consider an image  $x$  and its transformation  $g_T \cdot x$ .

$$K_{\text{FC}}(x, g_T \cdot x) = \sum_{i_x, i_y} \sum_k \left\langle \phi(B_{k, i_x, i_y} \cdot x), \phi(B_{k, i_x, i_y} \cdot g_T \cdot x) \right\rangle_{\Theta} \quad (77)$$

$$= \sum_{i_x, i_y} \sum_k \left\langle \phi(B_{k, i_x, i_y} \cdot x), \phi(g_T^{-1} \cdot B_{k, i_x, i_y} \cdot x) \right\rangle_{\Theta} \quad (78)$$

$$= \sum_{i_x, i_y} \sum_k \left\langle \phi(B_{k, i_x, i_y} \cdot x), \phi(B_{k, i_x - 1 \pmod n, i_y} \cdot x) \right\rangle_{\Theta} \quad (79)$$

It is clear that there is no change of variable that could make this kernel equal to  $K_{\text{FC}}(x, x)$ . In general,

$$K_{\text{FC}}(x, g_T \cdot x) \neq K_{\text{FC}}(x, x) \quad (80)$$

In other words, the fully connected convolutional network does not in general produce invariance to the translation transformation. Its kernel over an orbit is in general not constant.

To prove that  $K_{\text{FC}}$  is not, in general, rank-deficient, one can consider a seed image where only one pixel is active, and consider shifts in the images of size larger than the filter's size. Doing so results in a kernel matrix over the orbit that is a multiple of the identity, which is full rank.

□

**Proposition 2.** *The kernel matrix of a global average pooling convolutional network  $K_{\text{GAP}}$  over a translation orbit  $O_T$  is constant.*

*Proof.* We now study how a global average pooling layer affects the kernel. We consider two successive images from the translation orbit  $(x, g_T \cdot x) \in O_T$ :

$$K_{\text{GAP}}(x, g_T \cdot x) = \sum_{\substack{i_x, i_y \\ i'_x, i'_y}} \sum_k \left\langle \phi(B_{k, i_x, i_y} \cdot x), \phi(B_{k, i'_x, i'_y} \cdot (g_T \cdot x)) \right\rangle_{\Theta} \quad (81)$$

$$= \sum_{\substack{i_x, i_y \\ i'_x, i'_y}} \sum_k \left\langle \phi(B_{k, i_x, i_y} \cdot x), \phi(g_T^{-1} \cdot B_{k, i'_x, i'_y} \cdot (x)) \right\rangle_{\Theta} \quad (82)$$

$$= \sum_{\substack{i_x, i_y \\ i'_x, i'_y}} \sum_k \left\langle \phi(B_{k, i_x, i_y} \cdot x), \phi(B_{k, i'_x - 1 \pmod n, i'_y} \cdot (x)) \right\rangle_{\Theta} \quad (83)$$

By the change of variable with renaming  $i'_x \leftarrow i'_x - 1 \pmod n$ , we recover:

$$K_{\text{GAP}}(x, g_T \cdot x) = \sum_{\substack{i_x, i_y \\ i'_x, i'_y}} \sum_k \left\langle \phi(B_{k, i_x, i_y} \cdot x), \phi(B_{k, i'_x, i'_y} \cdot x) \right\rangle_{\Theta} \quad (84)$$

$$= K_{\text{GAP}}(x, x) \quad (85)$$

The kernel of a global average pooling convolutional network computed over a translation orbit is thus constant.

In our spectral error formula, the kernel over a pair of orbits will thus be rank-deficient (each orbit-wise block being constant), such that some inverse eigenvalues in the denominator will diverge. The spectral error will thus go to 0 (perfect generalization). We recover the well-known fact that a global average pooling convolutional network is invariant to translations.

□

**Proposition 3.** *The kernel matrix of a fully connected convolutional network  $K_{FC}$  over a rotation orbit  $O_R$  is circulant, but in general not rank-deficient or constant.*

*Proof.* Now we show that the kernel of a fully connected convolutional network is circulant over an orbit of image rotations. Consider a pair of images from this orbit  $(x, x') \in O_R$ . We show next that applying the same image rotation  $g_R$  to both these images leaves the kernel unaffected:

$$K_{FC}(g_R \cdot x, g_R \cdot x') = \sum_{i_x, i_y} \sum_k \left\langle \phi(B_{k, i_x, i_y} \cdot g_R \cdot x), \phi(B_{k, i_x, i_y} \cdot g_R \cdot x') \right\rangle_{\Theta} \quad (86)$$

$$= \sum_{i_x, i_y} \sum_k \left\langle \phi(g_R^{-1} \cdot B_{k, i_x, i_y} \cdot x), \phi(g_R^{-1} \cdot B_{k, i_x, i_y} \cdot x') \right\rangle_{\Theta} \quad (87)$$

Applying a rotation to image  $x$  is equivalent to applying a change of index to the convolutional filters  $B_{k, i_x, i_y}$  jointly with rotating the filters. We denote  $B'_{k, n-i_y, i_x} = g_R^{-1} \cdot B_{k, i_x, i_y}$ .

$$K_{FC}(g_R \cdot x, g_R \cdot x') = \sum_{i_x, i_y} \sum_k \left\langle \phi(B'_{k, n-i_y, i_x} \cdot x), \phi(B'_{k, n-i_y, i_x} \cdot x') \right\rangle_{\Theta} \quad (88)$$

We operate the changes of variable with renaming  $i_x \leftarrow n - i_y, i_y \leftarrow i_x$ .

$$K_{FC}(g_R \cdot x, g_R \cdot x') = \sum_{i_x, i_y} \sum_k \left\langle \phi(B'_{k, i_x, i_y} \cdot x), \phi(B'_{k, i_x, i_y} \cdot x') \right\rangle_{\Theta} \quad (89)$$

Assuming that the weights  $\Theta$  of the filters  $B_k$  are drawn from a random normal distribution  $B_k \sim \mathcal{N}(\mathbf{0}, \mathbf{I})$ , then  $B'_k = g_R^{-1} \cdot B_k$  will have the same distribution of weights  $B'_k \sim \mathcal{N}(\mathbf{0}, \mathbf{I})$ . Thus:

$$K_{FC}(g_R \cdot x, g_R \cdot x') = K_{FC}(x, x') \quad (90)$$

This concludes our proof that the kernel of a fully connected convolutional network is circulant over an orbit of image rotations.

Another question of interest is, is there anything special about the kernel of two images belonging to the same orbit. Consider an image  $x$  and its transformation  $g_R \cdot x$ .

$$K_{FC}(x, g_R \cdot x) = \sum_{i_x, i_y} \sum_k \left\langle \phi(B_{k, i_x, i_y} \cdot x), \phi(B_{k, i_x, i_y} \cdot g_R \cdot x) \right\rangle_{\Theta} \quad (91)$$

$$= \sum_{i_x, i_y} \sum_k \left\langle \phi(B_{k, i_x, i_y} \cdot x), \phi(g_R^{-1} \cdot B_{k, i_x, i_y} \cdot x) \right\rangle_{\Theta} \quad (92)$$

$$= \sum_{i_x, i_y} \sum_k \left\langle \phi(B_{k, i_x, i_y} \cdot x), \phi(B'_{k, n-i_y, i_x} \cdot x) \right\rangle_{\Theta} \quad (93)$$

There is no change of variable that could make this kernel equal to  $K_{FC}(x, x)$ . In general,

$$K_{FC}(x, g_R \cdot x) \neq K_{FC}(x, x) \quad (94)$$

In other words, the fully connected network does not produce invariance to the rotation transformation. Its kernel over an orbit is in general not constant.

A similar argument as in the case of shifts can be made to prove that the kernel is not, in general, rank-deficient. This can be obtained by choosing a ‘‘Dirac-like’’ image whose only active pixel is not at the center of the image.  $\square$

**Proposition 4.** *The kernel matrix of a global average pooling convolutional network  $K_{GAP}$  over a rotation orbit  $O_R$  is circulant, but in general not rank-deficient or constant.*

*Proof.* We study how changing the last layer from a fully connected to a global average pooling layer affects the results of the previous proposition.

$$K_{\text{GAP}}(g_R \cdot x, g_R \cdot x') = \sum_{\substack{i_x, i_y \\ i'_x, i'_y}} \sum_k \left\langle \phi(B_{k, i_x, i_y} \cdot g_R \cdot x), \phi(B_{k, i'_x, i'_y} \cdot g_R \cdot x') \right\rangle_{\Theta} \quad (95)$$

$$= \sum_{\substack{i_x, i_y \\ i'_x, i'_y}} \sum_k \left\langle \phi(g_R^{-1} \cdot B_{k, i_x, i_y} \cdot x), \phi(g_R^{-1} \cdot B_{k, i'_x, i'_y} \cdot x') \right\rangle_{\Theta} \quad (96)$$

$$= \sum_{\substack{i_x, i_y \\ i'_x, i'_y}} \sum_k \left\langle \phi(B'_{k, n-i_y, i_x} \cdot x), \phi(B'_{k, n-i'_y, i'_x} \cdot x') \right\rangle_{\Theta} \quad (97)$$

where we denote  $B'_{k, n-i_y, i_x} = g_R^{-1} \cdot B_{k, i_x, i_y}$  the filter rotated and displaced by the rotation. Changing variables as  $i_x \leftarrow n - i_y$ ,  $i_y \leftarrow i_x$ ,  $i'_x \leftarrow n - i'_y$ ,  $i'_y \leftarrow i'_x$ , we get

$$K_{\text{GAP}}(g_R \cdot x, g_R \cdot x') = \sum_{\substack{i_x, i_y \\ i'_x, i'_y}} \sum_k \left\langle \phi(B'_{k, i_x, i_y} \cdot x), \phi(B'_{k, i'_x, i'_y} \cdot x') \right\rangle_{\Theta} \quad (98)$$

$$= K_{\text{GAP}}(x, x') \quad (99)$$

The kernel of this network is thus circulant on a single orbit, as before with the fully connected convolutional network.

We now compute the kernel value for pairs of images belonging to the same orbit, in order to check whether the kernel is constant over an orbit:

$$K_{\text{GAP}}(x, g_R \cdot x) = \sum_{\substack{i_x, i_y \\ i'_x, i'_y}} \sum_k \left\langle \phi(B_{k, i_x, i_y} \cdot x), \phi(B_{k, i'_x, i'_y} \cdot g_R \cdot x) \right\rangle_{\Theta} \quad (100)$$

$$= \sum_{\substack{i_x, i_y \\ i'_x, i'_y}} \sum_k \left\langle \phi(B_{k, i_x, i_y} \cdot x), \phi(g_R^{-1} \cdot B_{k, i'_x, i'_y} \cdot x) \right\rangle_{\Theta} \quad (101)$$

$$= \sum_{\substack{i_x, i_y \\ i'_x, i'_y}} \sum_k \left\langle \phi(B_{k, i_x, i_y} \cdot x), \phi(B'_{k, n-i'_y, i'_x} \cdot x) \right\rangle_{\Theta} \quad (102)$$

Changing variables as  $i'_x \leftarrow n - i'_y$ ,  $i'_y \leftarrow i'_x$ , we get:

$$K_{\text{GAP}}(x, g_R \cdot x) = \sum_{\substack{i_x, i_y \\ i'_x, i'_y}} \sum_k \left\langle \phi(B_{k, i_x, i_y} \cdot x), \phi(B'_{k, i'_x, i'_y} \cdot x) \right\rangle_{\Theta} \quad (103)$$

$$\neq K_{\text{GAP}}(x, x) \quad (104)$$

In general, the kernel is not constant over an orbit.

To prove that this kernel over an orbit is in general not rank deficient, one can resort to using a seed image that is the sum of two ‘‘Dirac-like’’ images, each with a single nonzero pixel, and both of them in an area contained within the filter size.  $\square$

## D Varying the number of angles in an orbit

We report here plots comparing spectral and exact NTK errors for varying number of rotations for a 1 hidden layer MLP.

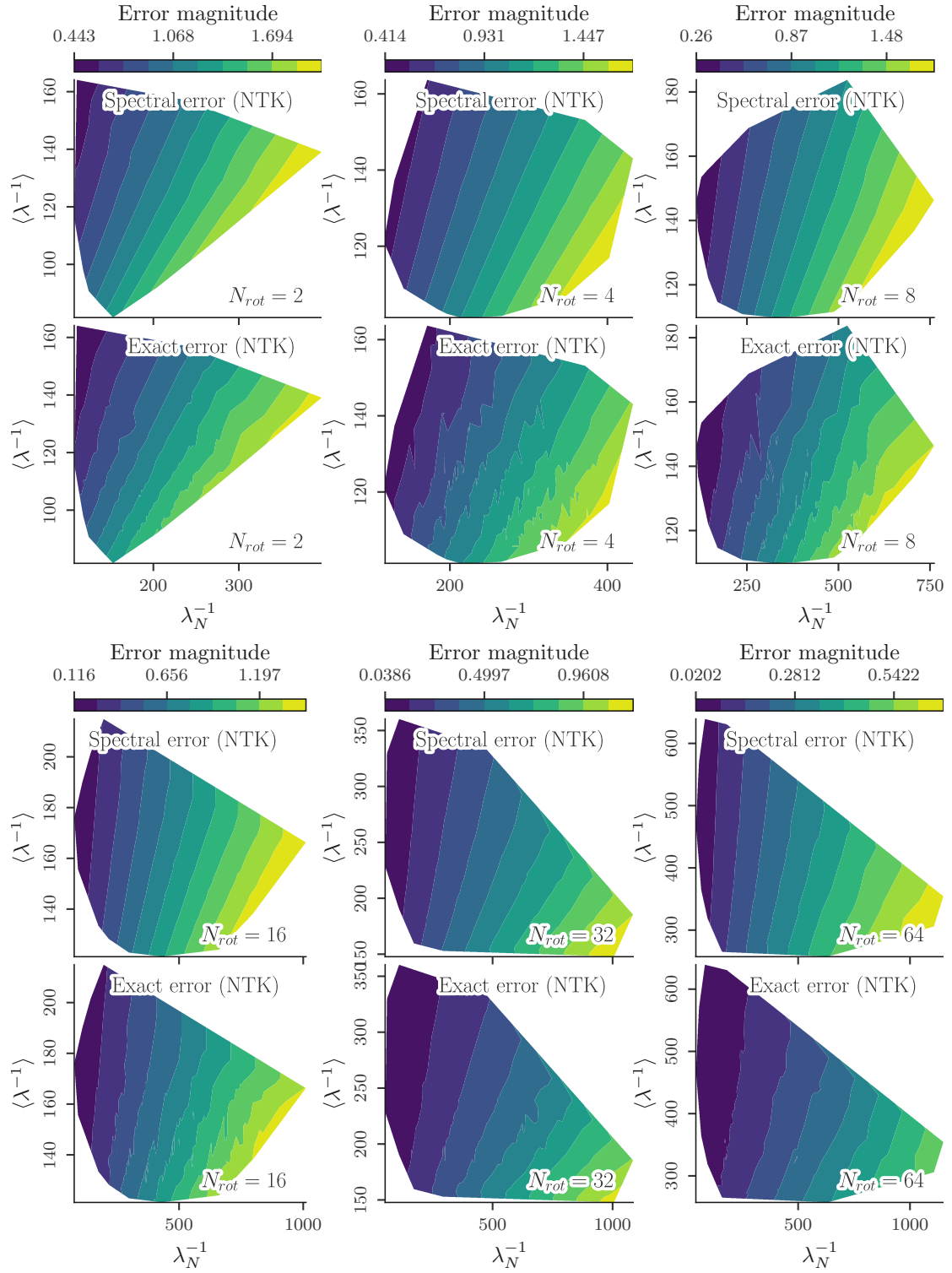


Figure 9. Comparison of spectral and exact NTK errors across a range of values for  $\lambda_N$  and  $\langle \lambda^{-1} \rangle$ .

## E Further MLP analyses

We report here plots of the NTK analysis for a deeper MLP (5 hidden layers, Fig. 10), and a MLP that is trained via Adam (Fig. 11).

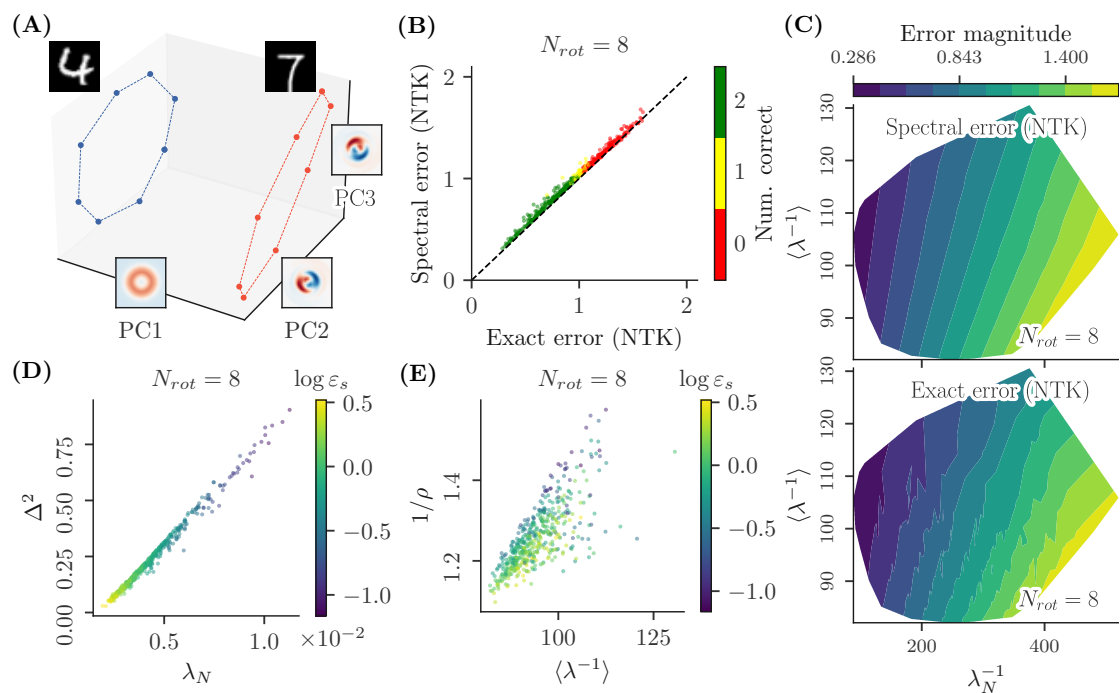


Figure 10. MLP, 5 hidden layers.

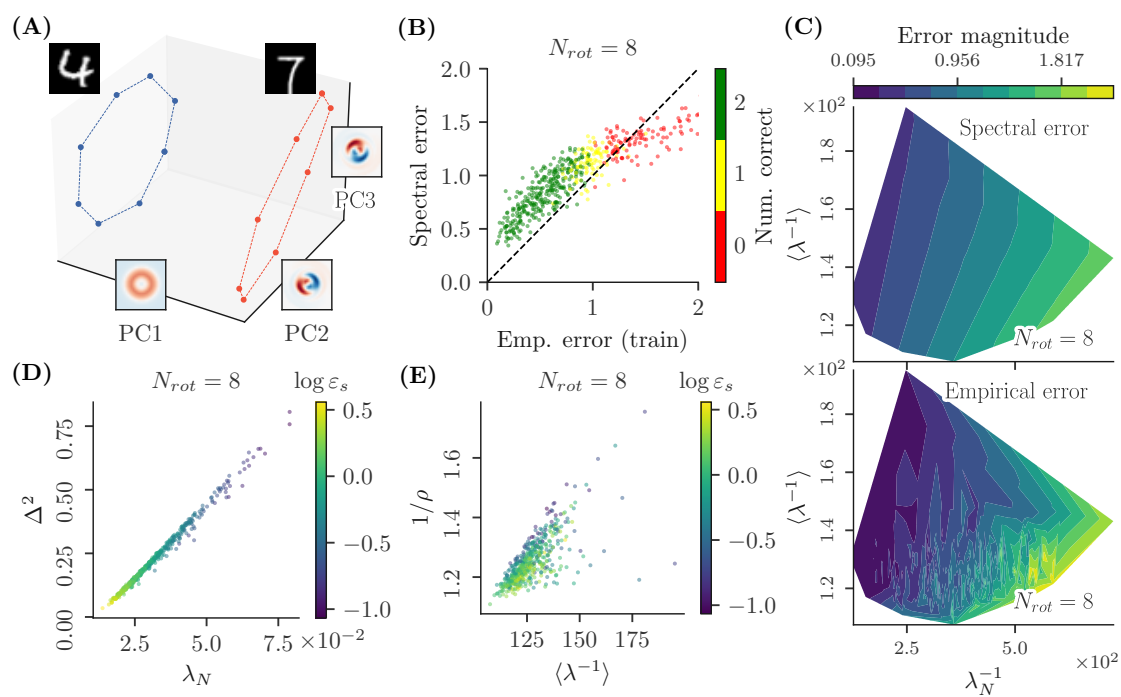


Figure 11. Trained MLP.

## F Multiple seeds, multiple classes - additional figures

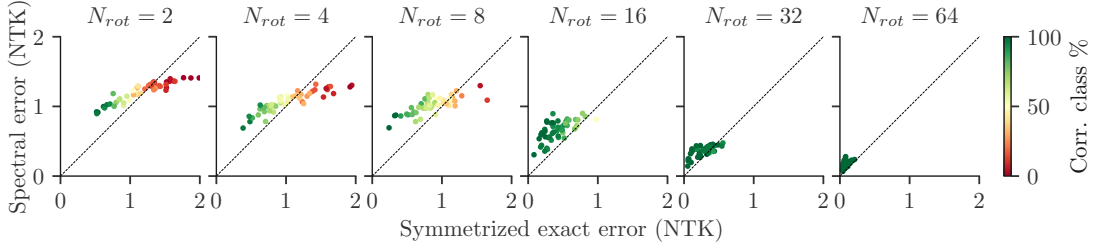


Figure 12. **Comparison of spectral and exact NTK errors for the multiple seeds case.** We compare the spectral error, averaged over all the pairings of orbits for a given number of pairs, and the symmetrized NTK prediction error, over a range of number of rotations in the orbits,  $N_{rot}$ . We superimpose the bisector as a visual reference. The color coding reflects the percentage of seeds (of both classes) for which the NTK regression gives a correct prediction, understood as agreeing with the +1 label of the missing points. As the number of points in the orbits increases, both errors decrease as expected, and the percentage of correct NTK predictions increases.

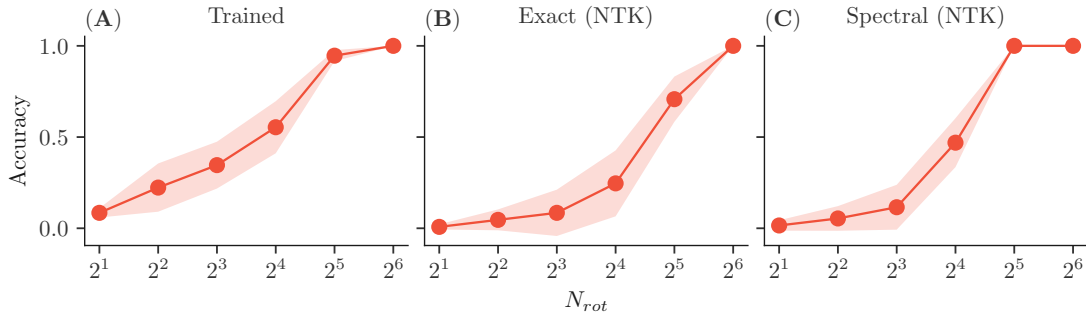


Figure 13. **Our spectral method correctly reproduces the generalization behavior of a trained finite-width MLP on rotated-MNIST, as we vary the number of sampled angles.** On a version of rotated-MNIST comprising all 10 classes and 13 seed images per class, we compare (A) a cross-entropy trained MLP (2 hidden layers) (B) a one-versus-all NTK regression strategy for this same architecture (we exclude one angle from one class and use NTK regression on the missing points, assuming label +1 for this class and label -1 for all other classes, repeat over all leave-out classes and average classification accuracy over all missing points), and (C) our multi-class adapted spectral error (see text). As the number of sampled angles in the orbits increases, the accuracies of all methods increase similarly and gradually on the missing points, showing that no mechanism for symmetry learning is present for the finite-width network that would be missing from our spectral theory, or from simple NTK regression.



## G Further Convolutional NTK (CNTK) analyses

### G.1 Rotation orbits

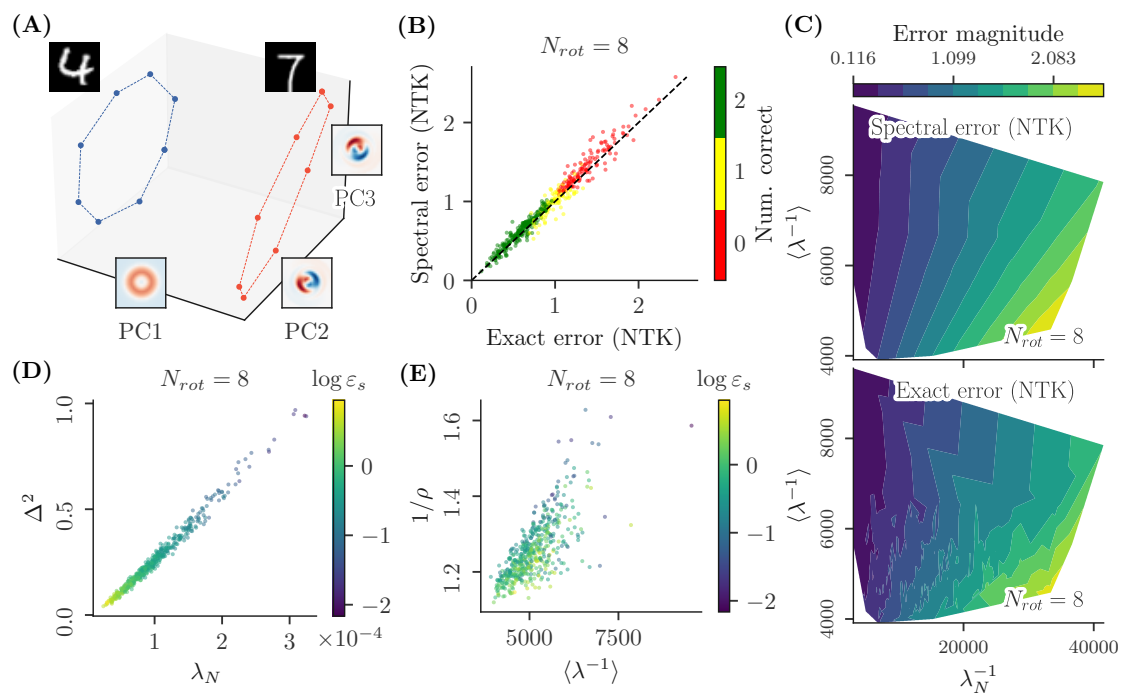


Figure 14. CNTK, fully connected, on rotation orbit.

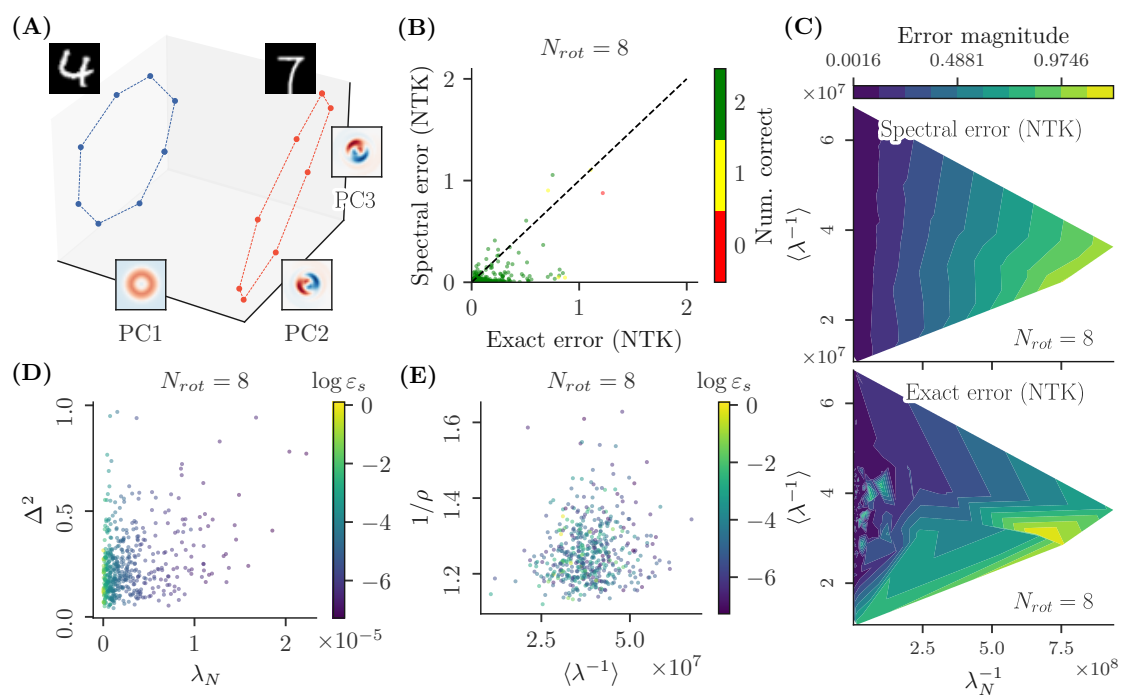


Figure 15. CNTK, Global Average Pooling, on rotation orbit.

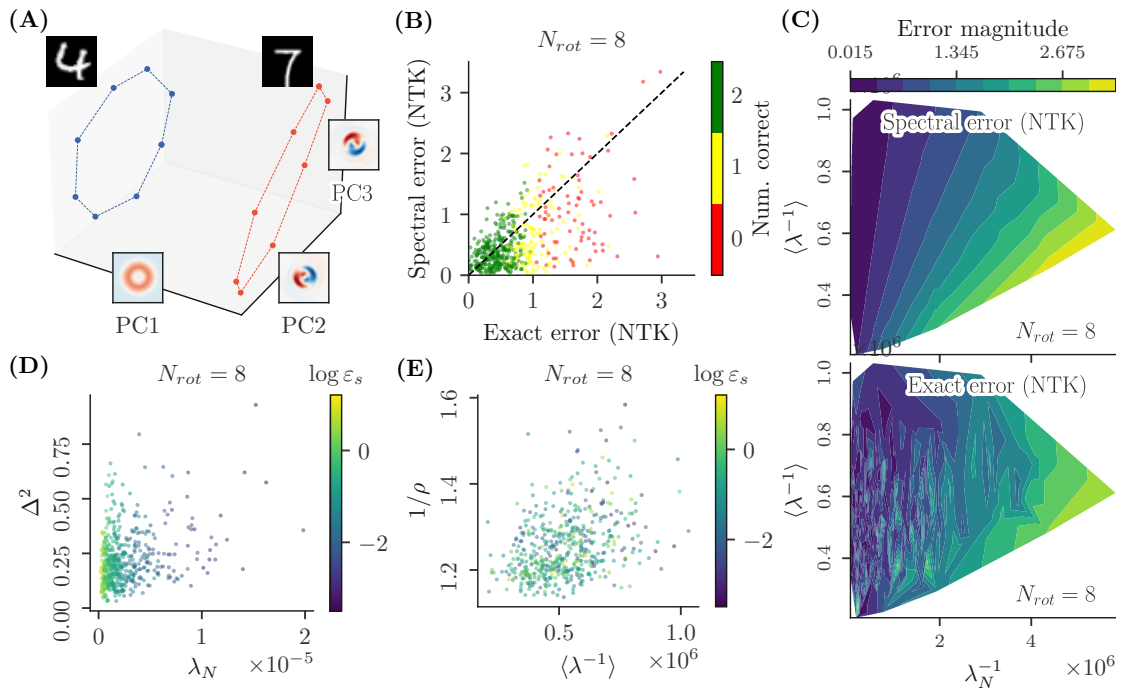


Figure 16. CNTK, Global Average Pooling, on rotation orbit. Kernel size (4, 4), strides (4, 4).

## G.2 Translation orbits

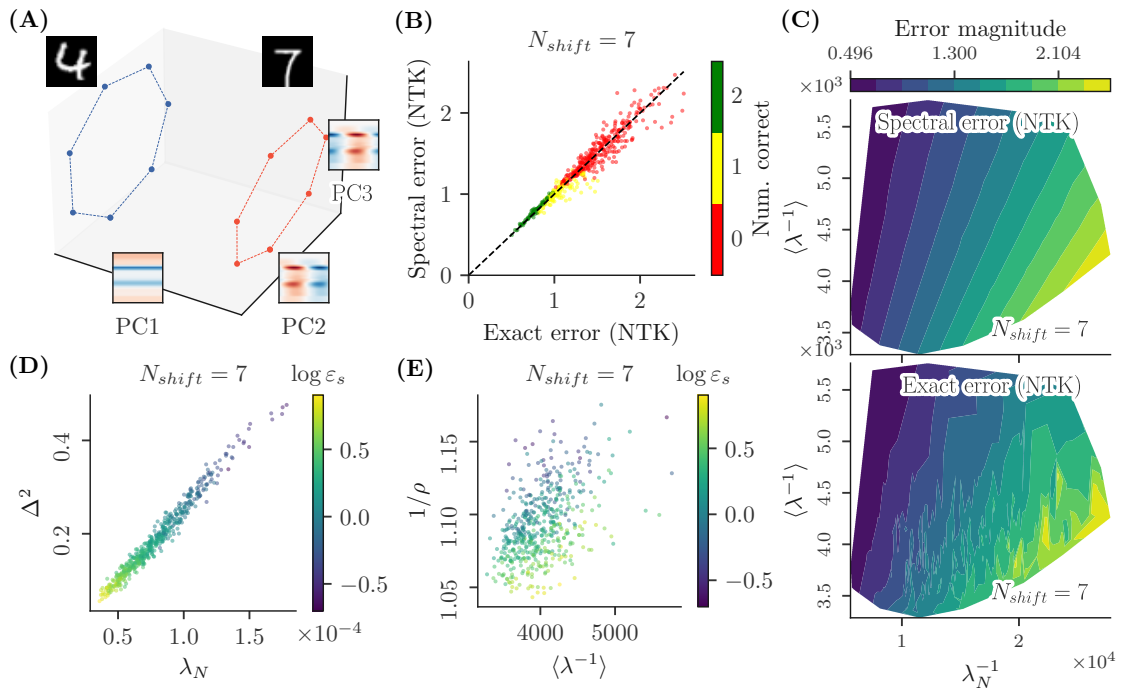


Figure 17. CNTK, Fully Connected, on translation orbit.

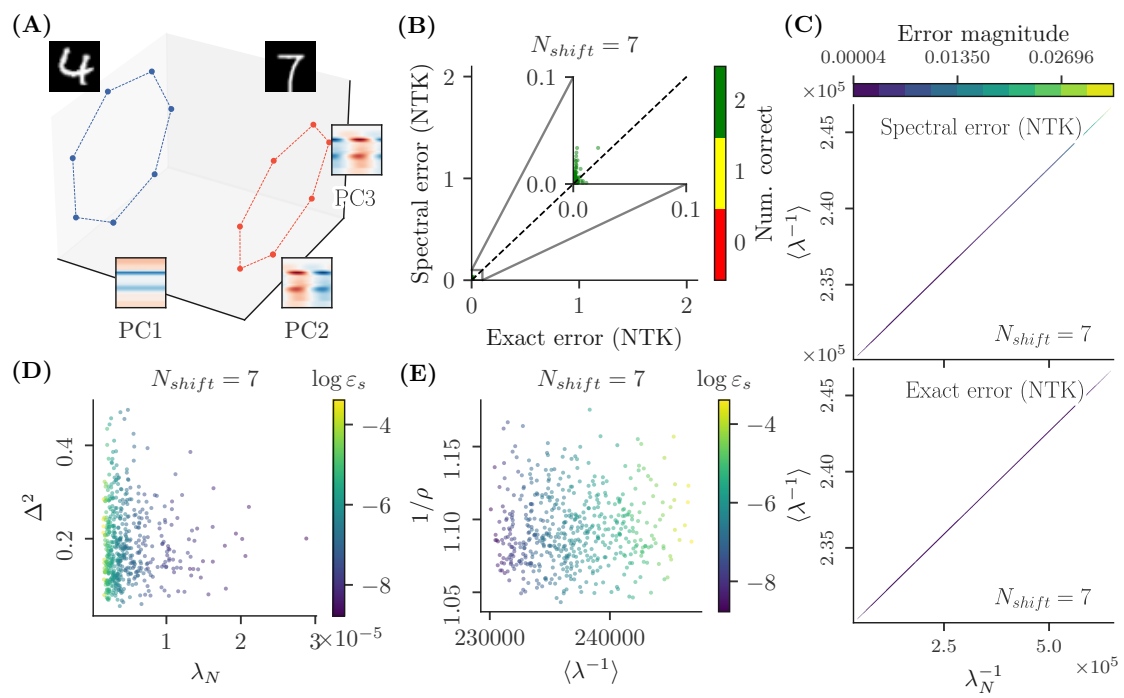


Figure 18. CNTK, Global Average Pooling, on translation orbit.